THE EFFECTS OF SEA ICE ON THE TIDES IN THE KITIKMEOT SEA: RESULTS USING YEAR–LONG CURRENT METER DATA FROM DEASE STRAIT AND TIDAL MODELS

by

Lina M. Rotermund
B. Sc. (Hons), Dalhousie University, 2016

A Thesis Submitted in Partial Fulfillment
of the Requirements for the Degree of

MASTER OF SCIENCE

in the Department of Physics and Astronomy

© Lina M. Rotermund, 2019
University of Victoria

All rights reserved. This thesis may not be reproduced in whole or in part, by photocopy or other means, without the permission of the author.

The effects of sea ice on the tides in the Kitikmeot Sea: results using year–long current meter data from Dease Strait and tidal models

Lina M. Rotermund
B. Sc. (Hons), Dalhousie University, 2016

Supervisory committee

Jody Klymak (Department of Physics and Astronomy)

Co-supervisor

William Williams (Department of Physics and Astronomy)

Co-supervisor

Abstract

We examine the tides in the Kitikmeot Sea using year-long time-series from moored instrumentation in Dease Strait, and a 3D barotropic numerical tidal model of the region. The in-situ data show strong tidal damping during wintertime seasonal sea ice cover, with a 50-60% reduction in M_2 and K_1 tidal elevation and 65% reduction in M_2 and K_1 tidal velocities at the sea ice maximum. We hypothesize the damping largely occurs in Victoria Strait, the eastern gateway of the Kitikmeot Sea, where tidal-induced ridging causes thick, rough ice to accumulate over its shallow sill. Using the numerical model, FVCOM, we independently vary sea ice friction and sea ice thickness, and show that the observed wintertime tidal damping likely requires both very rough ice and a partial sea ice blockage in the sill region.

Analysis of the model shows different dynamics and dissipation of the dominant M_2 and K_1 tides. Both M_2 and K_1 tides are dominated by the Atlantic tides entering through Victoria Strait. Arctic tides, entering from the west, have a minor, but significant, contribution to the M_2 tide. Overall, the K_1 tide, after 19% dissipation in Victoria Strait and 24% in adjoining bays, propagates far into the region and behaves as a Helmholtz resonator in Dease Strait and Coronation Gulf. In contrast, 92% of the M_2 tidal energy does not reach Dease Strait because, in addition to dissipation in Victoria Strait (29%), it is significantly diverted into adjoining bays and around an amphidrome in eastern Queen Maud Gulf. The K_1 tide, with double the wavelength of the M_2 tide, is less diverted.

Table of contents

List of tables

List of figures

Acknowledgments

I would like to thank my supervisors Bill Williams and Jody Klymak for their immense support and help throughout my master's degree. I have gained skills that will benefit me in future research endeavours. The Arctic field work also provided unique experiences that I am very grateful to have had. I would also like to thank crew members of the *R/V Martin Bergmann* for their valued assistance in field work and the researchers and oceanographic technicians of the Kitikmeot Sea Science Study for helpful discussions. Additionally, I would like to thank Yongsheng Wu for kindly providing the FVCOM outputs for the Kitikmeot Sea and Randy Scharien who provided data and assistance in understanding the sea ice dynamics of the region.

I would also like to acknowledge funding support from the Alexander Graham Bell CGS M NSERC award and University of Victoria donor awards (R.M. Pearce Memorial Fellowship, Commander Peter Chance MASC Graduate Fellowship and Bob Wright Graduate Scholarship). The research was also supported by the Arctic Research Foundation, Fisheries and Oceans Canada, and Polar Knowledge Canada.

Finally, I want to express gratitude to my family for their continuous love and support.

1. Introduction

1.1 Motivation: why are tides important?

The Canadian Arctic Archipelago (CAA) is a grouping of islands that form one of the gateways between the Arctic Ocean and the North Atlantic Ocean. The bathymetry of the CAA is complex, containing many shallow sills and narrow channels, resulting in complex tidal dynamics that have crucial implications in Arctic environments. Tidal currents influence sea ice distribution, thickness and concentration, by fracturing and mobilizing sea ice throughout the Arctic (Holloway and Proshutinsky, 2007; Heil et al., 2008; Luneva et al., 2015). Tidal interaction with bottom topography can significantly enhance vertical mixing, bringing subsurface heat to the surface and hindering the rate of sea ice growth. These processes result in the formation of convectively driven leads and polynyas, which are areas of open water surrounded by sea ice (Holloway and Proshutinsky, 2007; Williams et al., 2007; Hannah et al., 2009). Tidally-driven polynyas form in numerous locations across the CAA including at Hells Gate-Cardigan Strait, Dundas Island, Lambert Channel, Committee Bay, Fury and Hecla Strait (Hannah et al., 2009). Open water allows for roughly two orders magnitude greater exchange of heat between the atmosphere and ocean during winter (Williams et al., 2007). Including more accurate tidal models improves heat flux calculations of the Arctic Ocean (Holloway and Proshutinsky, 2007; Chen et al., 2009). Amplified upward mixing can also lead to higher nutrient fluxes towards the surface and localized elevated biological productivity (Williams et al., 2007; Hannah et al., 2009), leading to ecosystem hot spots.

Investigating the effect of sea ice on the tides is important, because tides can significantly enhance biological production. In the Kitikmeot Sea (in the southern CAA, Figure 1) primary productivity is relatively low (Varela et al., 2013) and new production is impeded due to the restricted inflow of nutrient-rich, salty, Pacific-origin water through the shallow-silled (< 30 m) straits that connect the region to the greater Arctic Ocean. Primary production is further limited

because the region receives large volumes of freshwater from mainland watersheds, resulting in a strong summer stratification between the surface freshwater and bottom salty water, which suppresses the upward mixing of dissolved nutrients. The Kitikmeot Sea contains several shallow sills and narrow straits where strengthened tidal flows occur which could have major ramifications on the local ecosystem. One area of early ice melt break up is around the Finlayson Islands, which are the primary constriction within Dease Strait (DS, the middle strait) connecting Coronation Gulf (CG, the western gulf) to Queen Maud Gulf (QMG, the eastern gulf) (Figure 1). Accurately representing the tides and their response to sea ice is critical to better understand such regions.

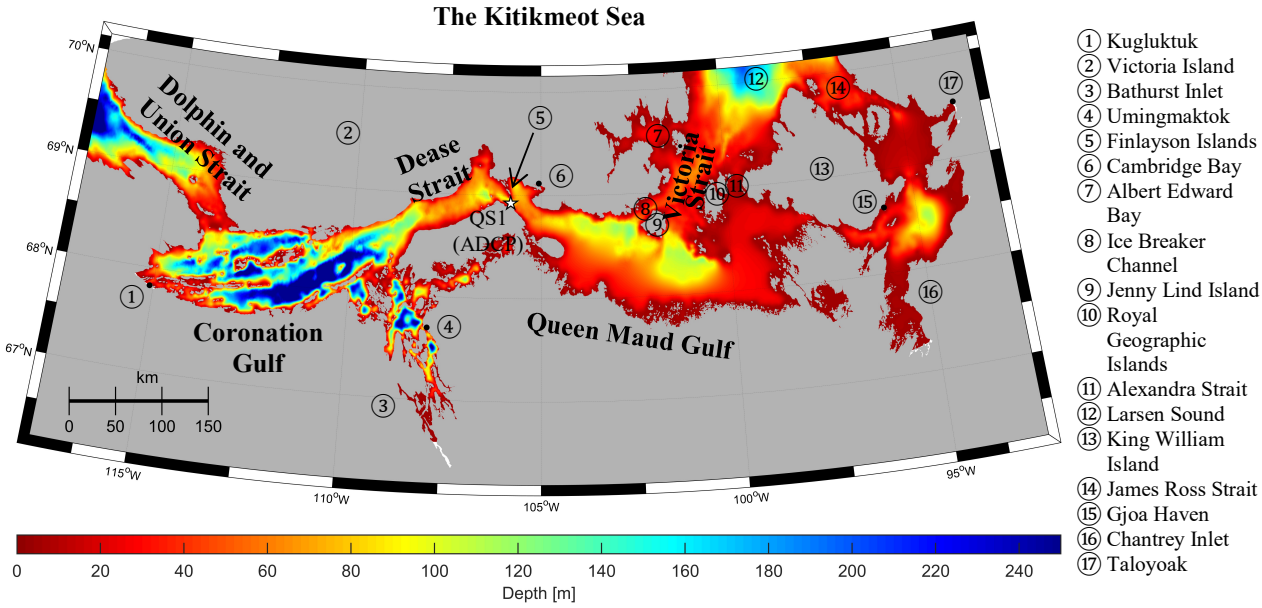

Figure 1. Map of the Kitikmeot Sea with in the southern Canadian Arctic Archipelago (CAA). The mooring is the white star labeled Qikirtaq South 1 (QS1) at longitude -105.816 and latitude 68.924. Important acronyms: Dolphin and Union Strait (DUS, the western strait), Dease Strait (DS, the middle strait), Victoria Strait (VS, the eastern strait), Coronation Gulf (CG, the western gulf) and Queen Maud Gulf (QMG, eastern gulf).

1.2 The role of sea ice cover on the tidal modification

In previous tidal models including the CAA, the tidal variability due to sea ice has been insignificant (smaller than the rms error of the predicted values) or tidal changes have only been several percent of the amplitude (Kagan and Sofina, 2010; Kagan et al., 2011; Kowalik, 1981;

Kowalik and Proshutinsky, 1993, 1994), therefore the ocean surface in models is often assumed to have no ice or have a static ice cover for the entire year (Collins et al., 2011; Kagan and Sofina, 2012; Kagan et al., 2010; Padman and Erofeeva, 2004). This may lead to tidal prediction programs (i.e. WebTide) not producing accurate tidal predictions throughout the year (Collins et al., 2011). Using the 2D barotropic T-UGOm (Toulouse Unstructured Grid Ocean Model, Pairaud et al., 2008), different ice coverage scenarios were modelled over the CAA resulting in no consistent improvements to the baseline case, so the baseline case was used as the final model (Collins et al., 2011). The baseline case used the average ice cover concentration of September 1989 and January 1990. The surface drag coefficient, $C_{surf} = C_{IO} \max\left(0, 2\left(A - \frac{1}{2}\right)\right)$, is based on ice cover concentration, A, and the sea ice friction coefficient [unitless], $C_{IO} = 18 \times 10^{-3}$. The four scenarios include ice coverage of the baseline case, a case using half the friction of the baseline, a case using the September ice cover and a case using the January ice cover (Collins et al., 2011). The South Central region (including Dease Strait, Queen Maud Gulf, and Victoria Strait) included some of the largest changes in the M_2 or K_1 tidal error depending on the scenario, which is possibly due to lack of resolution of the Finlayson Islands within Dease Strait (Collins et al., 2011). Error differences could also be due to seasonal changes in tides as proposed for the Southeast region (Gulf of Boothia). It was concluded that further observational research and improvements on the model are needed for those regions.

We will show that tides in the Kitikmeot Sea are reduced by over 50%, likely due to sea ice. Tidal modulation has been observed in other regions across the Arctic, but often to a lesser extent. The Hudson Bay System is a shallow, semi-diurnal resonant system, in which M_2 tidal amplitudes are damped from August to March by about 10% in western parts of Hudson Bay and up to 30 – 40% in eastern parts (Godin, 1985; Kleptsova and Pietrzak, 2018; Prinsenberg, 1988; St-Laurent et al. 2008), while tidal increases were observed in western Hudson Strait from August

to March (St-Laurent et al., 2008). The Hudson Bay System experiences seasonal phase shifts of up to 15° (St-Laurent et al., 2008). In the Kara Sea, with ice-cover the M_2 tidal amplitude is dampened by about 7% and the phase shifts 15° (Volkov et al., 2002). M_2 amplitude seasonal changes in the White Sea are also small, both winter increases and decreases of 7 – 9% are observed (Kulikov et al., 2018). Very large seasonal changes of 43% increase and 63% decrease in M_2 elevation within the Laptev and Chukchi Seas, respectively (Kulikov et al., 2018). Even some non-Arctic regions experience tidal modulation due to sea ice, such as the very shallow Hudson River estuary in which the M_2 tide was reduced by up to 42% (Georgas, 2012).

Multiple numerical modelling studies attribute sea ice cover to the aforementioned modulation in tidal observations, but also sometimes stratification, hydrological conditions and seasonal shifts in amphidromic points. For the Hudson Bay System, an ice-ocean coupled 3-D numerical model with an ice-ocean drag coefficient of $C_{IO} = 2 \times 10^{-3}$ (at z = -5) reproduced the March M_2 amplitude decreases and increases satisfactorily (St-Laurent et al., 2008). Sea ice friction causes the amphidromic points to shift, leading to larger changes in close proximately to these locations such as the eastern side (St-Laurent et al., 2008). A different model (STORMTIDE, Müller et al., 2012) in the same location obtained similar results using a value of $C_{IO} = 4.5 \times 10^{-3}$ (Müller et al., 2014). More recently, simulations using a time varying ice-field in a 2D barotropic ADCIRC model (ADvanced CIRCulation, Luettich and Westerink, 2004; Kleptsova and Pietrzak, 2018) showed significant tidal modulation throughout Hudson Bay System and within parts of the CAA, often close to amphidromic points. The surface drag coefficient parametrization is similar to Collins et al. (2011), $C_{surf} = C_{IO} \max\left(0, 2\left(A - \frac{1}{2}\right)\right)$, however now the ice cover, A, is time varying and $C_{IO} = 2.5 \times 10^{-3}$ or 18×10^{-3}. Kleptsova and Pietrzak (2018) compare their model to observations in Cambridge Bay, concluding that both values of C_{IO} underestimate the damping of the tidal elevation. In Tuktoyaktuk, Sachs Harbour, Ulukhaktok, and Kugluktok $C_{IO} = 18 \times 10^{-3}$

performs relatively well and in Churchill, Nain and Qaqortoq-Julianehab both values of C_{IO} overestimate the tidal damping (Kleptsova and Pietrzak, 2018). A different model using $C_{IO} = 15 \times 10^{-3}$ (3D finite element hydrothermodynamic model QUODDY-4, Kagan and Timofeev, 2006) showed pronounced seasonal variability of the M_2 tidal constant on the Siberian continental shelf, but insignificant changes in the Canadian parts of the Arctic Ocean (Kagan and Sofina, 2010). Sea ice blockages were not incorporated in the previously mentioned tidal models, but were in the model for the Hudson River estuary (2D version of NYHOPS model, Bruno et al., 2006; Georgas, 2012). Tidal changes in the Hudson River were a result of sea ice friction ($C_{IO} = 7.5 \times 10^{-3}$) and not due to the land-fast sea ice in areas shallower than 3.5 m (reducing cross sectional area of river mouth) or an increased sea ice volume (effective shallowing of the river depth by 1 m) (Georgas, 2012). One common conclusion amongst all modelling studies was that further research into tidal modulation due to sea ice is still required.

1.3 Outline

This paper addresses: how do the M_2 and K_1 tides behave within the Kitikmeot Sea? How does this system compare with simple analytical models? And how does sea ice friction or ridging affect tidal elevation and current amplitude and phase? Chapter 1: Introduction, emphasized the importance of understanding the link between the tides and sea ice by reviewing prior research relating to the seasonality of tides and sea ice. In Chapter 2: Methods, the site tides and sea ice concentration and thickness are provided. A description of the mooring instrumentation, the Finite–Volume Community Ocean Model (FVCOM), the sea ice parametrization and the varying simulation parameters are also specified. Chapter 3: Results, demonstrates that the year-long observational tidal ocean currents and elevation are reduced by over 50% from ice–free months to ice–covered months. Numerical modelling results are also analysed; the tidal dynamics are studied using FVCOM without and with sea ice friction and sea ice blockages. In addition, a 1D analytical model is also used to examine the tidal dynamics in the region. In Chapter 4: Discussion and

summary, seasonality in the broader CAA is briefly examined, limitations and future work are proposed, and in-situ data and model results are discussed and summarized.

2. Methods

2.1 Site description

2.1.1 Tides in the Kitikmeot Sea

The tides in the Kitikmeot Sea are not only unique because they are heavily influenced by sea ice, but also because the region is generally shallow and connected to the greater Arctic Ocean by two very shallow straits, one in the east and one in the west, which if either is blocked by sea ice could have significant impacts on tides in the region. Tides that have propagated through the Arctic Ocean, the Arctic tides, enter through Dolphin and Union Strait (DUS) in the west while the Atlantic tides enter through Victoria Strait (VS) in the east, interacting linearly and nonlinearly with each other in the region. The Atlantic tides have major roles in controlling the tides over most of the CAA, while the Arctic tides generally play only a minor role (Chen et al., 2009; Guo et al., 2018 (submitted)). As the tides enter the region they are damped by the shallow sills, resulting in mostly smaller tidal amplitudes compared to the other parts of the CAA. The dominant semidiurnal tidal constituent is the M_2 tide (principal lunar semidiurnal, 12.42 h period), and the dominant diurnal tidal constituent is the K_1 tide (lunar diurnal, 23.93 h period). The M_2 tide entering the Kitikmeot Sea from the west through DUS is not negligible, conversely, the K_1 tide entering from the west through DUS is negligible. The M_2 tide entering the Kitikmeot Sea from the east through VS forms an amphidromic point west of King William Island (Collins et al., 2011; Kleptsova and Pietrzak, 2018; Kagan and Sofina, 2012), while the K_1 tide, with double the wavelength compared to the M_2 tide, does not. Generally, the M_2 tidal elevation is larger than the K_1 tidal elevation with exception at the amphidromic point and in Coronation Gulf where the K_1 tide is larger than the M_2 tide. A more in-depth description and analysis of the K_1 and M_2 tides are provided in section 3.2 using our FVCOM simulation, as it has higher resolution around the Finlayson Islands compared to the tidal models of Collins et al. (2011), Kleptsova and Pietrzak (2018) and Kagan and Sofina

(2012). In our model we also vary the levels of sea ice friction, and employ sea ice blockages in DUS or VS to examine the unique effects sea ice has on the tides in the Kitikmeot Sea.

2.1.2 Sea ice in the Kitikmeot Sea

Dampened tidal amplitude during the winter months in the Kitikmeot Sea is hypothesized to be a consequence of both sea ice friction and sea ice ridging in Victoria Strait. A general understanding of the sea ice concentration, thickness and ridging in the region is provided to help implement sea ice friction and sea ice blockages in FVCOM.

Victoria Strait and Larsen Sound have thicker sea ice and a shorter ice free season than Coronation and Queen Maud Gulf. Coronation and Queen Maud Gulf have partial or full ice coverage for 10 months of the year which is dominated by thinner first-year ice (FYI) and no thicker multi-year ice (MYI) (Figure 2). Comparatively, Larsen Sound and Victoria Strait have partial or full ice coverage consisting of FYI but also 30% MYI for 11 months of the year.

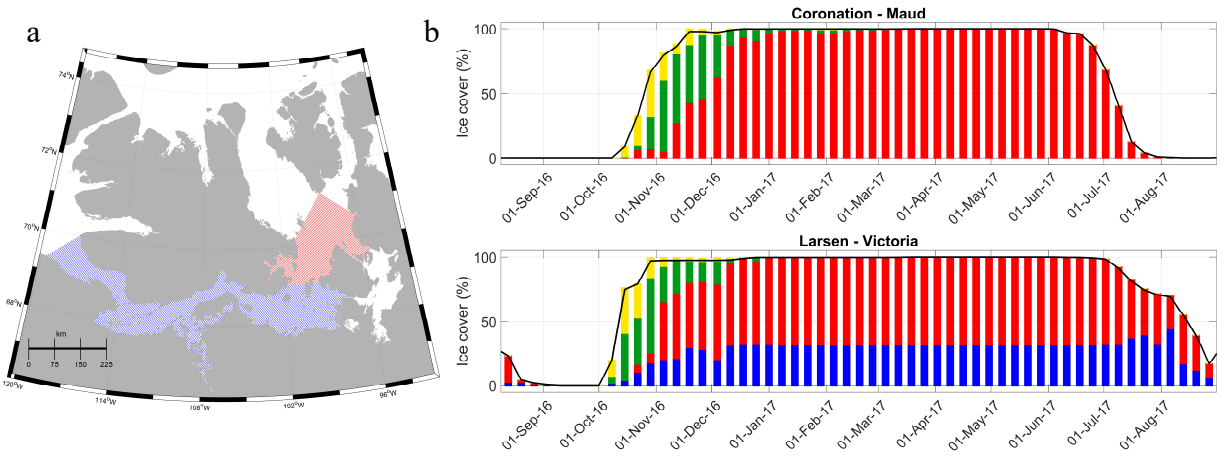

Figure 2. (a) Map of area coverage for Coronation and Queen Maud Gulf (shaded blue) and Larsen Sound and Victoria Strait (shaded red) and a time series of ice coverage showing thinner ice within (b) Coronation and Queen Maud Gulf compared to (c) Larsen Sound and Victoria Strait. Legend: new ice (yellow), young ice (green), first-year ice (FYI, red) and old ice/ multi-year ice (MYI, blue). Data obtained from the Canadian Ice Service (Iceweb1.cis.ec.gc.ca, 2019).

Sea ice thickness surveys carried out by airborne laser and electromagnetic induction (AEM) in May 2011, April 2015 (Haas et al., 2009; Haas and Howell, 2015) and April 2016 show

thick sea ice ridges in Victoria Strait. AEM measures snow and ice thickness together; snow thickness averages 0.2 – 0.4 m in the region (Melling, 2002). AEM will occasionally underestimate the maximum thickness of pressure ridges (Johnston and Haas, 2011; Haas and Howell 2015). Haas and Howell (2015) measured a mean ice thickness of about 2.5 m within Victoria Strait and Queen Maud Gulf (75% quartile = 2.75 – 2.96 m). Thicker ice piled up against the land-fast ice in the southern region of Victoria Strait, where the ice remained mobile until beginning of February 2015, resulting in vigorous deformation (Haas and Howell, 2015). Ice thickness measured in April 2016 show similar thickness measurements, averaging 2.64 m (std = 1.40 m) along the entire transect and averaging 3.32 m (std = 1.62 m) within the blockage area in Victoria Strait (Figure 3). Within the blockage area the 75% quartile is 3.9 m and the mean of the upper 25% is 5.4 m (std = 1.8 m) and of the upper 1% is 12.0 m (std = 2.0 m) (Figure 3). There are no ice thickness measurements in the winter of 2017.

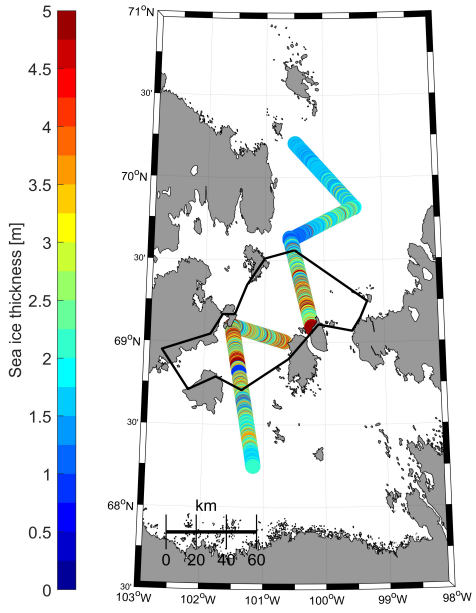

Figure 3. Sea ice thickness measurements via airborne laser and electromagnetic induction (AEM) on 08-Apr-2016 show thicker sea ice within Victoria Strait. The black line indicates the area used as the blockage in FVCOM.

Sentinel-1 synthetic aperture radar (SAR) imagery (C-band frequency) of Victoria Strait shows mobile ice conditions from the beginning of ice formation in October until March 2017,

which leads to strong sea ice deformation and ridging, resulting in thicker sea ice (Figure 4). SAR images taken on 04-Jan-2017, 14-Feb-2017 and 16-Feb-2017 show a lot of ice motion during the time period of about a month (Figure 4 a to b) and over two days (Figure 4 b to c). Each SAR image shows different open water fractures in the sea ice. In addition, they show patterns of low backscatter (dark pixels), representative of relatively smooth FYI, and high backscatter (bright pixels), representaive of more deformed, rougher, and thicker ice (Dierking, 2013). Insenity of C-band SAR backscatter is determined primarily by the ice surface roughness for FYI, and surface and volume scattering from MYI. The latter effect is due to the penetration of radar energy into the fresh, low density, upper layers of the MYI, and scattering from voids and inclusions. Brighter MYI floes are seen in the top right hand corner (Figure 4). Within Victoria Strait, Alexandra Strait and Ice Breaker Channel the brighter areas indicate rougher/thicker FYI due to stronger deformation. The blockage area within FVCOM outlines the brighter pixels (red dashed line, Figure 4c). Within the region of the blockage there are multiple shallow sills ranging between 5 – 25 m, hence major ice motion that produces thick sea ice can signficanly affect the depth of the water column and therefore the tides.

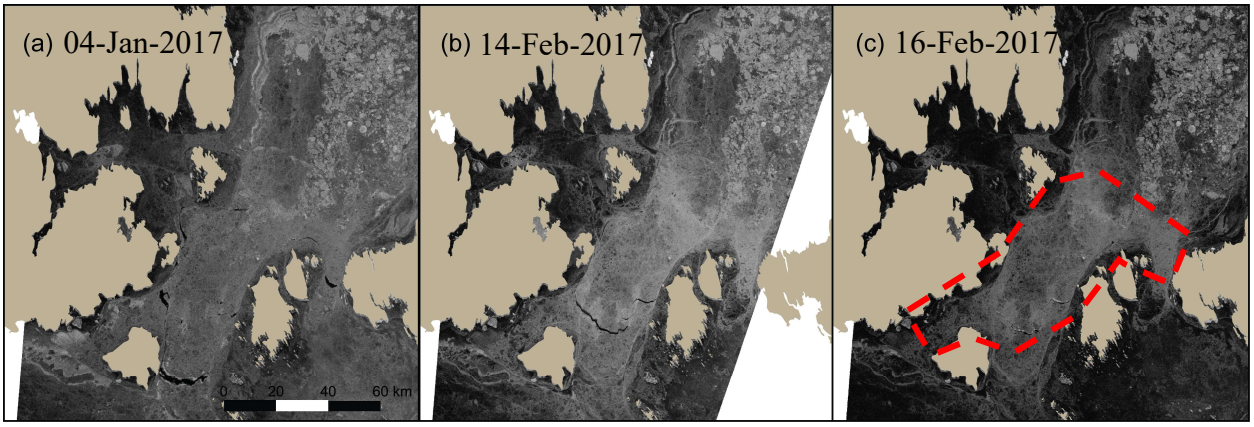

Figure 4. Sentinel-1 synthetic aperture radar (SAR) images showing sea ice movement within Victoria Strait region between (a) 04-Jan-2017, (b) 14-Feb-2017, and (c) 16-Feb-2017. The darker pixels are smooth, thin ice, the brighter pixels are rougher, thicker ice. The blockage area within FVCOM is outlined by the red dashed line.

2.2 Mooring instrumentation

A multi-instrument mooring was deployed by the Kitikmeot Sea Science Study aboard the Arctic Research Foundation's *R/V Martin Bergmann* near the Finlayson Islands for one year from 09-Aug-2016 to 30-Aug-2017 (Qikirtaq South 1 QS1, Figure 1) to measure ocean currents and stratification. This position was chosen for being both the deepest location and the greatest constriction within Dease Strait. The mooring was equipped with an acoustic Doppler current profiler (ADCP) and three Seabird MicroCats measuring pressure, salinity and temperature. Only the ADCP data are presented here. Current and pressure data were obtained from an upward facing moored RDI Sentinel V100 (300 kHz) ADCP, 1 m above the sea floor at a depth of 108 m. The ADCP was configured at burst intervals of 15 minutes, consisting of 40 pings at 2 second intervals. The bin sizes are 2 m in the vertical. A second shipboard ADCP combined with a GPS compass was used to calibrate the orientation of the moored ADCP. During the calibration, ocean currents were measured by the shipboard ADCP every 3 h over a 27 h period (19:00 17-Aug-2017 to 00:00 19-Aug-2017), in order to resolve one tidal cycle. This led to a 48.9° rotation of the moored ADCP to match the onboard ADCP measurements. Data above the sea surface and within the sidelobe reflection shadow were rejected. During ice cover there were a lack of scatters in the upper 30 m, so to reduce the noise the velocities were averaged over 1 hour time intervals, which is sufficient for tidal analysis.

2.3 Finite-Volume Community Ocean Model (FVCOM)

2.3.1 Model description

The model used for the tidal dynamics of the Kitikmeot Sea is the Finite-Volume Community Ocean Model (FVCOM), a three-dimensional (3D), finite-volume, unstructured triangular grid mesh system, ice-ocean coupled circulation model (Chen et al., 2003, 2006). The model solves the 3D mass continuity and momentum, salinity and temperature equations and

employs 2.5 Mellor-Yamada (M-Y) turbulence closure model in the vertical and a Smagorinsky diffusivity closure scheme in the horizontal. FVCOM uses a finite volume integration method based on a flexible unstructured triangle mesh system allowing higher resolution in areas of interest, i.e. resolving the Finlayson Islands, unlike other tidal models. The model domain spans the region in which sea ice effects are the strongest, so the open boundaries do not see as much tidal modulation as the inner gulfs, see section 4.1 for further details. The model domain is from Larsen Sound, the eastern open boundary, through to the western end of Dolphin and Union Strait (DUS), the western open boundary, spanning 900 km of water pathways (Figure 1), which incorporates James Ross Strait, Chantrey Inlet, Ice Breaker Channel, Alexandra Strait, Albert Edward Bay, Victoria Strait (VS) in the eastern domain, Queen Maud Gulf (QMG), Dease Strait (DS), Bathurst Inlet, Coronation Gulf (CG) in the central regions, and DUS and in the western domain. The region also covers several hamlets including Cambridge Bay, Gjoa Haven, Tayoloak and Kugluktuk. Depths range from 5 m at the coast lines to 460 m in western DUS (Figure 1). The topographic data used in the model are a combination of the international bathymetric charts of the Arctic Ocean, Canadian Hydrographic Service data, and multibeam data. The total number of the triangular elements and nodes in the domain are 80166 and 43186, respectively. The horizontal resolution of model mesh varies from 200 m in narrow channels, close to coastlines and islands to about 10 km in the relatively open water. In the vertical direction, there are 21 sigma layers with high vertical resolution near the surface and bottom. This paper highlights the winter season, when stratification is relatively weak. Therefore the model uses barotropic tides, ignoring density effects, thus salinity and temperature are kept constant with depth and in horizontal space at 35 and 18 °C, respectively. The model was forced at the open boundaries with the tidal harmonic constants derived from the TPXO9 global tidal model (Egbert and Erofeeva, 2002), including tidal constituents of M_2, S_2, N_2, O_1, K_1, K_2, P_1 and Q_1. The open boundaries were both equally adjusted to match September conditions of the ADCP data by using the amplitude ratio and phase difference

of the tidal constituents at the mooring site, so the M_2, S_2, N_2, O_1, K_1, and K_2 tides at the boundary were multiplied by 1.6, 1.1, 1.5, 0.5, 0.5, and 1, respectively, and the phases shifted by -1, -15, 16, 7, 6, and 140°, respectively. The open boundaries were then kept constant for all simulations, only the sea ice parameterisation varied. The model was run from an initial still condition with a spin-up of 5 days at 4 s time steps and output at hourly intervals.

2.3.2 Simulation dynamics and drag coefficient

In this study, the friction of sea ice is described with the method of Wu et al. (2014, 2015):

$$\frac{\partial \boldsymbol{u}}{\partial t} + (\boldsymbol{u} \cdot \nabla)\boldsymbol{u} = -\frac{1}{\rho_o}\nabla P - 2\boldsymbol{\Omega} \times \boldsymbol{u} + \boldsymbol{F_r} - \lambda|\boldsymbol{u}|\boldsymbol{u}\, g(z) \qquad (1)$$

Here $\boldsymbol{u} = (u, v)$ is the tidal velocity, t is time, ρ_o is average density of the water column, P is pressure, $2\boldsymbol{\Omega} \times \boldsymbol{u}$ is the Coriolis acceleration where $\boldsymbol{\Omega}$ is the angular velocity of the earth, and $\boldsymbol{F_r}$ are the horizontal and vertical viscosity terms. The last term on the right-hand side characterizes the sea ice drag and is applied to the model elements in the horizontal and the sigma levels in the vertical and has been previously used in models to study fish cages and tidal power extraction (Wu et al., 2014, 2015). In our simulations, ice drag is implemented as a body force over a certain depth from the surface, denoted as h in Table 1, so that sea ice is within the water column. The body force is quadratic in velocity, $\boldsymbol{u}$, with a drag coefficient, per depth, given by λ [m^{-1}] and a step function, $g(z)$, in both horizontal and vertical coordinates which is equal to zero in areas of no sea ice and one in the presence of sea ice. For most of the simulations, we implement this sea ice formulation to be similar to a surface drag by setting the thickness of the body force region to h = 1 m. If the model had infinite vertical discretization, and minimal shear near the surface, then $h\lambda$ would approximately be equal to a surface quadratic drag coefficient, noted as C_{IO} [unitless] when referring to drag co-efficient values in the introduction (C_{IO} was mentioned in section 1.2). We use this specification rather than a surface drag so that we can have much thicker values of h that represent ice blockages (i.e. simulations G – I, Table 1). However, the numerical implementation

of the body force doesn't account for partial depth cells, so that the effective h is really the thickness of the number of vertical grid cells that encompass h, and hence $h_{eff} > h$. The mismatch is modest through much of the domain because we have substantial resolution near the surface. Further, we are really interested in comparing various orders of drag coefficients, so the numerical imprecision was deemed acceptable.

The drag coefficient is dependent on constants such as the roughness length, floe shape, ridge draft, slope of the ridge, distance between ridges and more (Lu et al., 2011; Tsamados et al., 2014), all difficult to measure in-situ quantities. Instead, values of C_{IO} are commonly tuned to match model results with observations. The ice-ocean drag coefficient ranges between $0.00132 < C_{IO} < 0.0268$ (Pease et al., 1983; Langleben, 1982; Madsen and Bruno, 1986; St-Laurent et al., 2008). We use ice-ocean drag coefficient values of λ = 0, 0.002, 0.004, 0.01, 0.02 and 0.03 m^{-1} to a depth of h = 1 m. An additional simulation with λ = 0.02 m^{-1} to a depth of h = 2 m was also executed. Any grid points where sea ice blockages were implemented had a very high λ value of 0.6 m^{-1} in order to represent the obstacle as impermeable. Outside of the blockage region a background drag of λ = 0.01 m^{-1} to a depth of 1 m was used. Table 1 summarizes the varying parameters for all 11 FVCOM runs.

Table 1. The varying sea ice parameters for each of the 11 FVCOM simulations. All simulations include both eastern and western forcing except simulation J.

Model run	λ [m^{-1}]	h [m]	Notes
A	0	–	–
B	0.002	1	–
C	0.004	1	–
D	0.01	1	–
E	0.02	1	–
E1	0.02	2	–
F	0.03	1	
G	0.01	1	Sea ice blockage in Victoria Strait (VS). The sea ice blockage has a thickness of 5.4 m.
H	0.01	1	Sea ice blockage in VS. The sea ice blockage has a thickness of 12 m.
I	0.01	1	Sea ice blockage in Dolphin and Union Strait (DUS) The sea ice blockage has a thickness of the water depth – 5 m.
J	0	–	No forcing from the western side.

3. Results

3.1 Observations

3.1.1 Year-long analysis of tidal elevation and currents at QS1 (Dease Strait)

Water elevation at mooring QS1 (Figure 5a) is dominated by the semi-diurnal band (M_2, S_2, N_2, ~2 cycles per day [cpd]), but also has peaks within the diurnal band (K_1, O_1, Q_1, ~1 cpd), and detected peaks at high frequencies (Figure 6a). Conversely currents (Figure 5b) at this location are dominated by the diurnal band, but also have peaks within the semi-diurnal band and smaller peaks at high frequencies (Figure 6b). The high frequency peaks around 2.9, 3.9, 4.9, and 5.9 cpd are the higher harmonics of the MK_3, M_4, $2MK_5$ and $2MS_6$, respectively, which are categorized as overtides or shallow water tides because they are caused by nonlinear mechanisms of the other tidal constituents in shallow bathymetry. An increase in the continuum around the peaks, known as tidal cusps (Munk et al., 1965), are observed at frequencies of 2, 2.9 and 3.9 cpd (Figure 6a). Tidal cusps arise from energy transfer from the major constituents into neighbouring frequencies, due to the variability of the tidal amplitudes, which is likely a result of sea ice in this region (Kulikov et al., 2018). The tidal currents are along channel, therefore the clockwise (CW) and counter-clockwise (CCW) components of the rotary spectra (Foreman and Henry, 1989) are approximately equal in energy across the frequency spectrum (Figure 6b). The tidal currents at mooring QS1 do not change significantly with depth, with exception in the ice-free months where wind can influence the surface currents, as seen at the beginning of October (Figure 5). Therefore, in all following analyses containing currents, the baroclinic tides are assumed negligible and depth averaged currents are used.

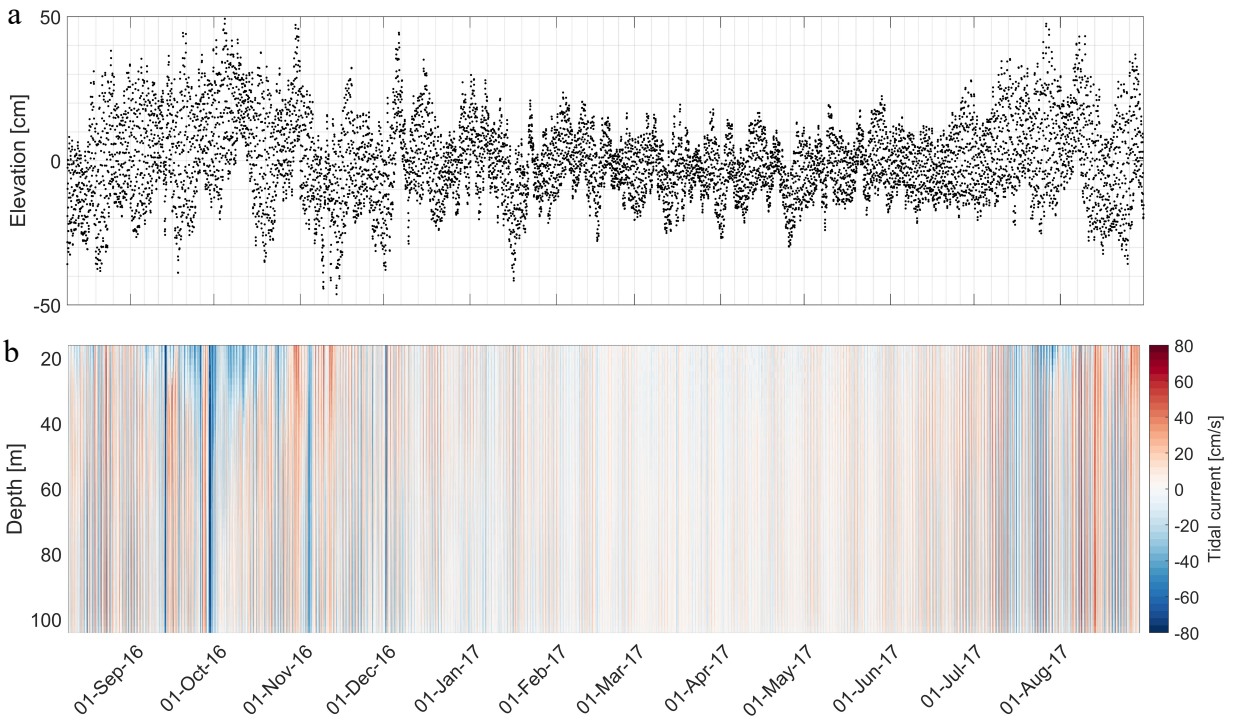

Figure 5. (a) Tidal elevation and (b) tidal current at the QS1 mooring in Dease Strait from 09-Aug-2016 to 30-Aug-2017. (b) The tidal current is along the semi-major axis of the current ellipse (positive axis is 168° counter clockwise from the due east).

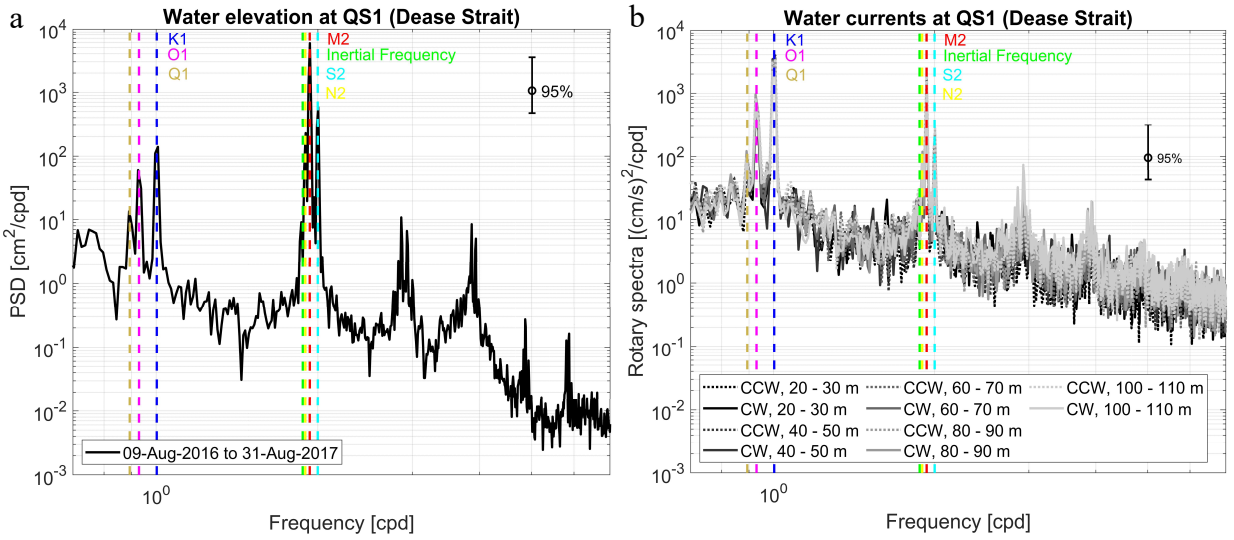

Figure 6. Welch's power spectral density (PSD) estimate for (a) water elevation and (b) water current (in 10 m depth averages) at mooring QS1 over the entire year-long series. The current contribution is the sum of one counter-clockwise (CCW) and one clockwise (CW) rotating vector. The PSD uses a Kaiser window of half overlap and the number of discrete Fourier transform (DFT) points set to N = 2048. Vertical dashed lines indicate frequencies of tidal constituents, K_1, O_1, Q_1, M_2, S_2, N_2 and the inertial frequency.

Standard tidal analysis (Pawlowicz et al., 2002) of seasonally modulated constituents made over a year will falsely place energy into harmonics of neighbouring frequencies, therefore inaccurately portraying the tides. The harmonic analysis determined the tidal elevation constituents with a signal to noise ratio (SNR) of 2 or greater in order of decreasing amplitude to be, M_2, S_2, SA, H_2, H_1, K_1, N_2, O_1, K_2, and T_2 (top 10 of Table 2) and tidal current constituents in order of decreasing amplitude (semi-major axis of the tidal ellipse) to be K_1, M_2, O_1, P_1, S_1, PSI_1, S_2, SA, H_2, and H_1 (top 10 of Table 3). For both tidal elevation and current the magnitude of the H_2 and H_1 amplitudes are 20 – 30% of M_2 amplitude, which is unrealistically large as astronomical forcing would indicate these components should typically be a couple of percent. Foreman and Neufeld (1991) suggest this is caused by energy leakage from the major constituent into neighbouring frequencies due to non-tidally driven changes in elevation such as atmospheric forcing (wind and temperature), stratification, or in this region, seasonal sea ice. Given the phasing of the annual cycle shown below, we attribute the seasonal modulation to sea ice.

Table 2. Tidal constituents with a signal to noise ratio (SNR) of 2 and greater from t-tide harmonic analysis on year-long detrended tidal elevation (ADCP depth) at mooring QS1 from Aug. 2016 - 2017.

Tidal constituent	Period (h)	Frequency (h^{-1})	Amplitude (cm)	Phase (°)	SNR
M_2	12.42	0.0805	12.71 ± 0.2	171 ± 1	5700
S_2	12	0.0833	4.37 ± 0.2	234 ± 3	610
SA	8764	0.0001	3.21 ± 2	253 ± 40	2
H_2	12.4	0.0806	2.65 ± 0.2	79 ± 4	250
H_1	12.44	0.0804	2.64 ± 0.2	112 ± 4	190
K_1	23.93	0.0418	2.52 ± 0.2	142 ± 4	180
N_2	12.66	0.079	2.36 ± 0.2	129 ± 4	230
O_1	25.82	0.0387	1.79 ± 0.2	335 ± 6	100
K_2	11.97	0.0835	1.46 ± 0.2	235 ± 10	35
T_2	12.02	0.0832	0.86 ± 0.2	337 ± 20	20
R_2	11.98	0.0835	0.85 ± 0.1	334 ± 10	35
L_2	12.19	0.082	0.67 ± 0.2	205 ± 20	18
PSI_1	23.87	0.0419	0.65 ± 0.2	117 ± 10	15
Q_1	26.87	0.0372	0.65 ± 0.2	49 ± 20	18
P_1	24.07	0.0415	0.65 ± 0.2	297 ± 20	12
MO_3	8.39	0.1192	0.63 ± 0.1	132 ± 9	30
NU_2	12.63	0.0792	0.62 ± 0.2	137 ± 20	12
S_1	24	0.0417	0.55 ± 0.2	270 ± 20	8
MK_3	8.18	0.1222	0.42 ± 0.1	237 ± 10	17
M_4	6.21	0.161	0.42 ± 0.1	8 ± 20	19
MKS_2	12.39	0.0807	0.40 ± 0.2	115 ± 40	3
$2N_2$	12.91	0.0775	0.38 ± 0.2	94 ± 20	6
RHO_1	26.72	0.0374	0.36 ± 0.2	290 ± 30	4
MS_4	6.1	0.1639	0.35 ± 0.1	57 ± 20	9
SO_3	8.19	0.1221	0.33 ± 0.1	192 ± 20	7
LDA_2	12.22	0.0818	0.27 ± 0.2	350 ± 30	2
MU_2	12.87	0.0777	0.28 ± 0.2	184 ± 40	3
MK_4	6.09	0.1642	0.22 ± 0.1	114 ± 40	2
MN_4	6.27	0.1595	0.07 ± 0	123 ± 20	11
$2MK_5$	4.93	0.2028	0.06 ± 0	4 ± 20	8
$2MS_6$	4.09	0.2445	0.04 ± 0	289 ± 30	6
M_6	4.14	0.2415	0.04 ± 0	357 ± 30	3
$2MK_6$	4.09	0.2445	0.04 ± 0	357 ± 30	2.6

Table 3. Tidal constituents with a SNR of 2 and greater from t-tide harmonic analysis on year-long detrended tidal currents (ADCP velocity) at mooring QS1 from Aug. 2016 - 2017.

Tidal constituent	Period (h)	Frequency (h^{-1})	Semi-major axis (cm/s)	Semi-minor axis (cm/s)	Inclination (°)	Phase (°)	SNR
K_1	23.93	0.0418	16.8 ± 0.7	1.1 ± 0.3	170 ± 1	148 ± 2	610
M_2	12.42	0.0805	8.6 ± 0.2	1.1 ± 0.1	165 ± 1	252 ± 2	1800
O_1	25.82	0.0387	8.3 ± 0.8	0.1 ± 0.4	170 ± 2	33 ± 5	120
P_1	24.07	0.0415	5.1 ± 0.6	0.2 ± 0.3	168 ± 3	137 ± 8	69
S_1	24	0.0417	4.4 ± 0.9	0.04 ± 0.4	167 ± 5	282 ± 10	22
PSI_1	23.87	0.0419	3.5 ± 0.7	-0.2 ± 0.3	175 ± 4	10 ± 10	29
S_2	12	0.0833	3.1 ± 0.3	0.3 ± 0.2	162 ± 3	313 ± 4	150
SA	8764	0.0001	2.7 ± 0.6	-0.1 ± 0.9	69 ± 20	235 ± 10	22
H_2	12.4	0.0806	2.5 ± 0.2	0.3 ± 0.2	171 ± 3	155 ± 6	150
H_1	12.44	0.0804	2.3 ± 0.2	0.02 ± 0.1	162 ± 4	186 ± 5	130
Q_1	26.87	0.0372	2.0 ± 0.7	-0.05 ± 0.3	170 ± 9	321 ± 20	8
PI_1	24.13	0.0414	1.9 ± 0.6	-0.3 ± 0.2	166 ± 10	229 ± 20	9
N_2	12.66	0.079	1.7 ± 0.2	0.2 ± 0.2	167 ± 5	203 ± 8	55
MF	327.9	0.0031	1.2 ± 0.7	0.5 ± 0.5	7 ± 40	259 ± 60	2
PHI_1	23.8	0.042	1.1 ± 0.7	-0.4 ± 0.2	180 ± 20	73 ± 40	3
TAU_1	25.67	0.039	0.9 ± 0.5	-0.04 ±0.3	150 ± 20	182 ± 30	4
SSA	4382	0.00023	0.9 ± 0.5	-0.3 ±0.9	76 ± 90	229 ± 50	4
K_2	11.97	0.0835	0.9 ± 0.3	-0.2 ± 0.2	7 ± 20	185 ± 20	7
T_2	12.02	0.0832	0.8 ± 0.2	0.03 ± 0.2	170 ± 10	36 ± 20	10
R_2	11.98	0.0835	0.7 ± 0.2	-0.1 ± 0.1	174 ± 10	65 ± 20	11
MKS_2	12.39	0.0807	0.7 ± 0.3	0.03 ± 0.3	142 ± 20	214 ± 20	7
NU_2	12.63	0.0792	0.6 ± 0.2	0.2 ± 0.1	166 ± 20	207 ± 31	8
MU_2	12.87	0.0777	0.4 ± 0.2	0.1 ± 0.2	7 ± 30	282 ± 42	3
L_2	12.19	0.082	0.4 ± 0.2	0.1 ± 0.2	150 ± 30	301 ± 30	4
M_4	6.21	0.161	0.4 ± 0.1	-0.05 ± 0.1	5 ± 10	111 ± 20	9
MS_4	6.1	0.1639	0.3 ± 0.1	-0.04 ± 0.1	171 ± 10	5 ± 20	7
SO_3	8.19	0.1221	0.3 ± 0.1	-0.2 ± 0.1	99 ± 50	351 ± 50	7
MK_3	8.18	0.1222	0.2 ± 0.1	-0.1 ± 0.1	114 ± 40	25 ± 40	6
MK_4	6.09	0.1641	0.2 ± 0.1	-0.05 ± 0.1	68 ± 80	28 ± 60	2
$2MK_5$	4.93	0.2028	0.13 ± 0.04	0.1 ± 0.1	80 ± 40	19 ± 40	9
M_6	4.14	0.2415	0.1 ± 0.1	-0.03 ± 0.04	1 ± 20	177 ± 30	6
$2MS_6$	4.09	0.2445	0.1 ± 0.1	-0.05 ± 0.04	23 ± 30	205 ± 30	5
$2SM_6$	4.05	0.2469	0.1 ± 0.1	-0.004±0.04	23 ± 30	288 ± 40	2
$2MK_6$	4.09	0.2446	0.1 ± 0.1	-0.1 ± 0.1	100 ± 100	51 ± 80	2

3.1.2 Seasonality in tidal elevation and currents at QS1 (Dease Strait)

During ice covered months the power spectral density is reduced compared to periods without sea ice. A 40-day spectral analysis was performed on both tidal elevation and barotropic tidal currents during ice-free periods, and during the maximum ice cover. Sea ice extent across the entire Arctic reaches a maximum between beginning and mid-March and a minimum mid-September (Nsidc.org, 2019). The energy at the diurnal and semidiurnal frequencies is decreased at maximum ice cover (01-Mar-2017 to 09-Apr-2017) compared to the ice-free periods (20-Aug-2016 to 28-Sep-2016, 23-Jul-2017 to 31-Aug-2017) (Figure 7). This decrease in energy indicates seasonal modulation of the tides, likely due to sea ice.

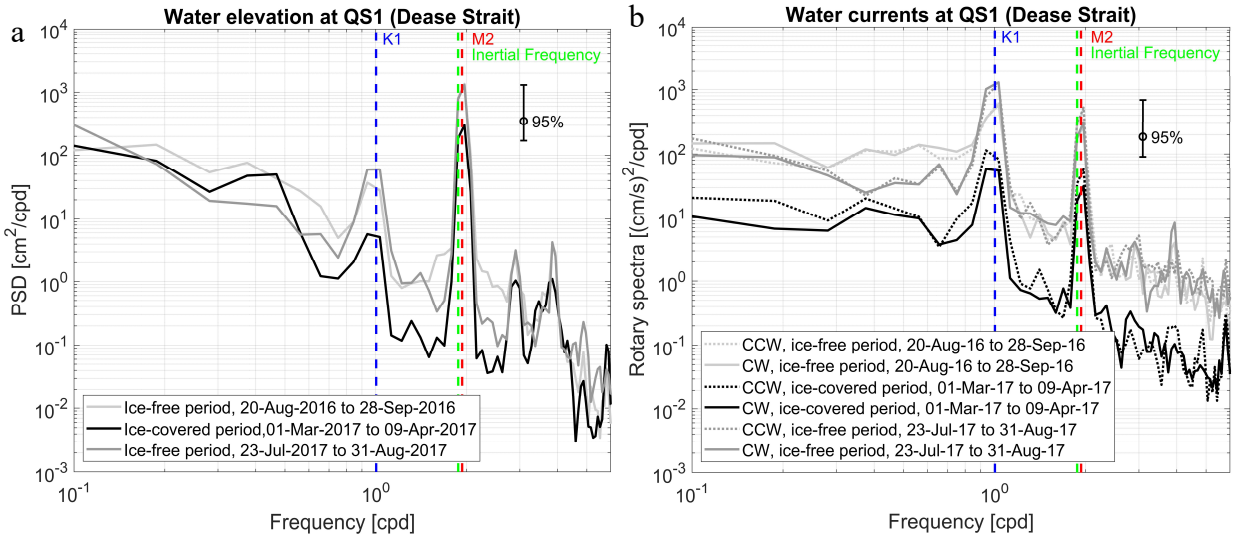

Figure 7. Welch's power spectral density estimate with a Kaiser window for (a) water elevation and (b) the depth averaged current over three time periods: ice-free period (20-Aug to 28- Sept 2016), maximum ice cover (01-Mar to 09-Apr 2017) and again ice-free period (23 Jul to 31 Aug 2017). Vertical dashed lines indicate frequencies of K_1 and M_2 tides, and the inertial frequency.

The M_2, S_2, N_2, K_1 and O_1 tidal elevation amplitudes decrease 49 - 62% from the ice-free period to the period of maximum ice cover and the phase varies seasonally by 0 - 13° (Figure 8). Tidal current amplitudes are damped by about 35 - 80% from the ice-free periods to the period of maximum ice cover, and the phase varies seasonally by 10 - 21° (Figure 9). Seasonal modulation

in the tide was estimated by computing tidal harmonic analysis in periods of 1.5 months with a 0.75 month overlap (Figure 8 and 9). The P_1 (K_2) tide was inferred from K_1 (S_2) tide in order to diminish their semi-annual beat frequency. The inference values used were the amplitude ratio and phase difference between P_1 (K_2) and K_1 (S_2) from the harmonic analysis of the year long time series. Comparing the initial ice-free period (centered around 01-Sep-2016) to maximum ice cover (centered around 06-March-2017), shows that for tidal elevation (Figure 8) the M_2 elevation amplitude is reduced by 52% (9.5 cm) and its phase shifts seasonally by -13 ± 2°. The K_1 elevation amplitude is damped by 58% (2.0 cm) and its phase shifts by 7 ± 16°, though the level of uncertainty partially hides this non-seasonal variability. For tidal currents (Figure 9) the M_2 amplitude is reduced by 65% (8.7 cm/s) and its phase shifts seasonally by -10 ± 4° and the K_1 amplitude is reduced by 65% (16.5 cm/s) and its phase shifts seasonally by 21 ± 9°. For both tidal elevation and currents, the semidiurnal constituent phases are shifted negatively, while the diurnal constituent phases are shifted positively from the initial ice-free period to the period of maximum ice cover. Both tidal elevation and current have clear seasonal changes likely due to sea ice.

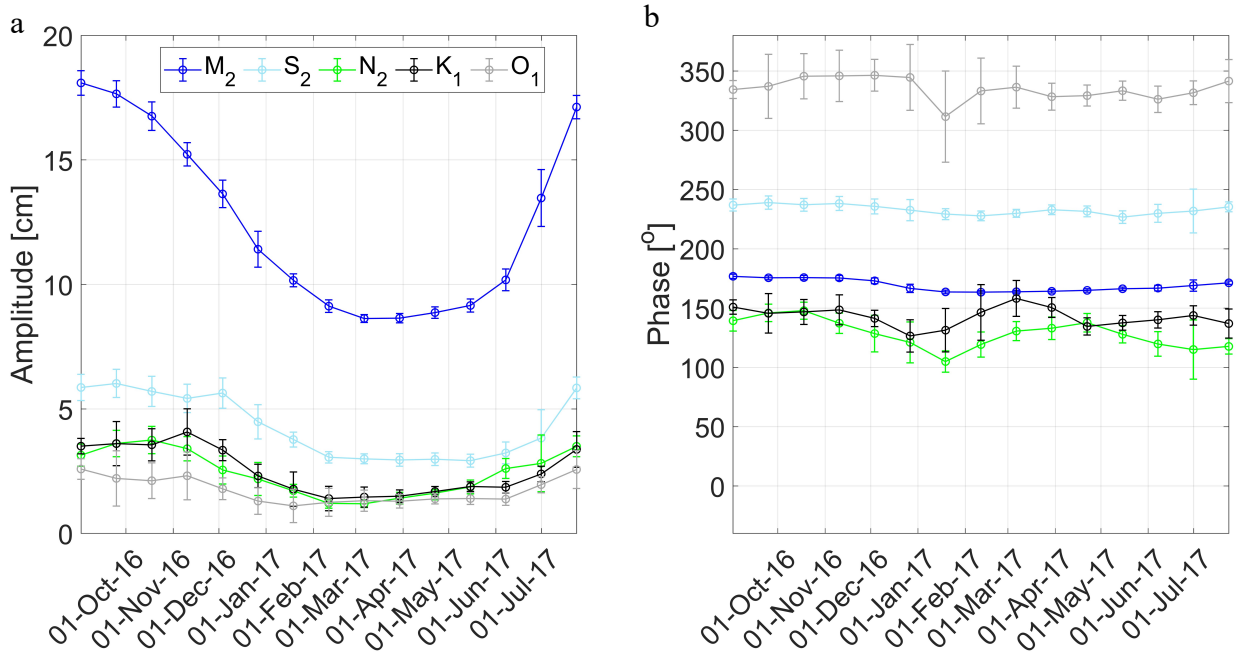

Figure 8. Seasonal dampening of the M_2 (blue), S_2 (light blue), N_2 (green), K_1 (black) and O_1 (gray) tidal water elevation (a) amplitude and (b) phase, both with 95% confidence intervals. T-tide was used to perform the tidal analysis on 1.5-month intervals with an overlap of 0.75 months.

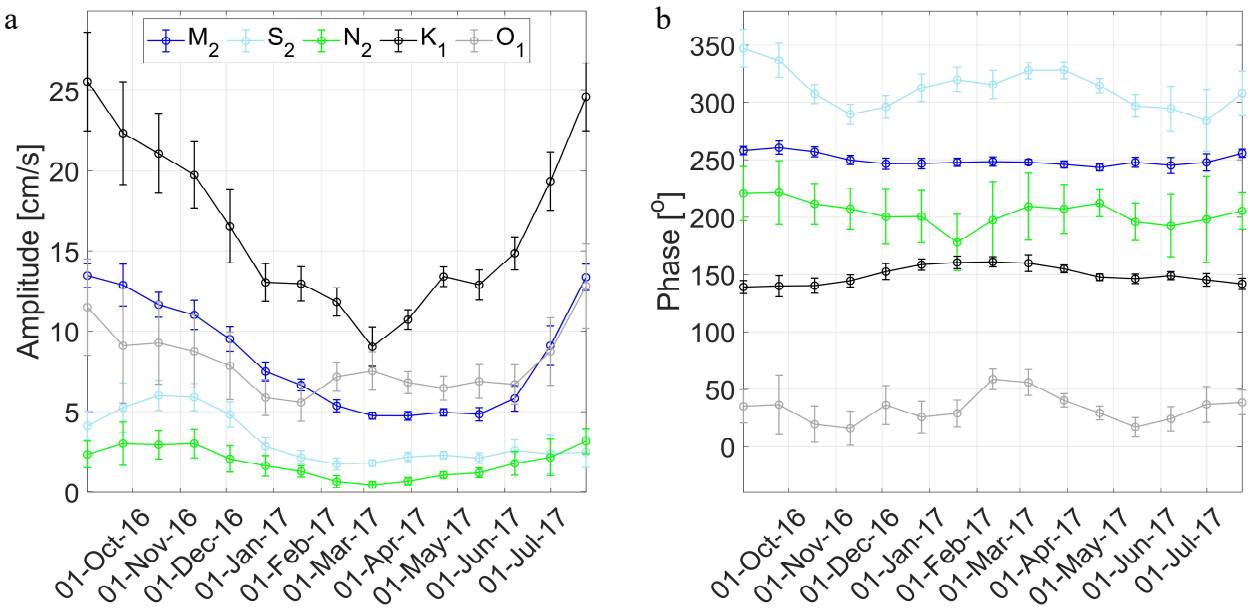

Figure 9. Seasonal dampening of the M_2 (blue), S_2 (light blue), N_2 (green), K_1 (black) and O_1 (gray) tidal water current (a) amplitude and (b) phase, both with 95% confidence intervals. T-tide was used to perform the tidal analysis on 1.5-month intervals with an overlap of 0.75 months.

3.2 Tidal FVCOM results

3.2.1 FVCOM results without sea ice friction (λ = 0 m^{-1})

FVCOM was employed to examine the effects of sea ice on tidal dynamics in the Kitikmeot Sea. Simulation A (λ = 0 m^{-1}) models the tidal dynamics during ice-free conditions (Figure 10, Table 4), Simulation A shows improvement over WebTide results when comparing tidal constituents to the September ADCP observations at QS1. Here a new version of WebTide was used, which utilizes a grid including bathymetry for the Finlayson Islands. The models, FVCOM and WebTide, were compared to the ADCP observations by calculating the error (Collins et al., 2011; Kleptsova and Pietrzak, 2018):

$$error = \left|A_o e^{i\varphi_o} - A_m e^{i\varphi_m}\right| \quad (2)$$

Here A and φ are the tidal constituent amplitude and phase, respectively. The subscript o denotes observed (ADCP data) and m denotes model. Using the values in Table 4, the K_1 and M_2 tidal elevation errors improve by 5.3 cm and 8.6 cm, respectively, compared to WebTide. The error for

K_1 and M_2 tidal currents improves minimally by 0.9 cm/s and 2.9 cm/s, respectively. This leads to a 3.4 ± 0.1 cm and 18.3 ± 0.6 cm error for K_1 and M_2 tidal elevation, and a 14.6 ± 11.0 cm/s and 11.3 ± 5.8 cm/s error for K_1 and M_2 tidal currents for FVCOM simulation A.

The K_1 and M_2 tides behave very differently upon entering the Kitikmeot Sea. These differences will be highlighted in the following paragraphs using the spatial patterns of the tidal amplitudes, phases, energy flux and dissipation rates (Figures 10 – 15). Using the linearized shallow water equations, one can describe the vertically-integrated energy flux for barotropic tides averaged over a tidal cycle by (Henry and Foreman, 2001):

$$\bar{F} = \sqrt{\bar{F_x}^2 + \bar{F_y}^2} \tag{3}$$

$$\{\bar{F_x}, \bar{F_y}\} = \frac{1}{2}\rho g H\{u_0\eta_0\, cos(\varphi_\eta - \varphi_u), v_0\eta_0\, cos(\varphi_\eta - \varphi_v)\} \tag{4}$$

Where ρ is average density of the water column, g is the gravitational acceleration, H is local water column depth, u_0, v_0, η_0 and φ_u, φ_v, φ_η are the amplitudes and phases of the tidal velocities, u, v, and tidal elevation, η: $u = u_0\cos(\omega t - \varphi_u)$, $v = v_0\cos(\omega t - \varphi_v)$ and $\eta = \eta_0\cos(\omega t - \varphi_\eta)$. $\omega = 2\pi/T$, where T is the period of the tidal constituent and t is time. Dissipation rates were estimated by calculating the divergence of the averaged energy flux field (Egbert and Ray 2001). The changes in amplitude and phase are shown along a transect (solid black line in Figure 12) spanning the Kitikmeot Sea (Figure 14) beginning at the eastern open boundary (x = 0 km) and extending until the western open boundary (x = 1013 km) of the model domain. At locations denoted by the black dashed lines in Figure 12, the energy flux was integrated across the channel and graphed with respect to the distance along the transect within the Kitikmeot Sea (Figure 13 and Figure 15).

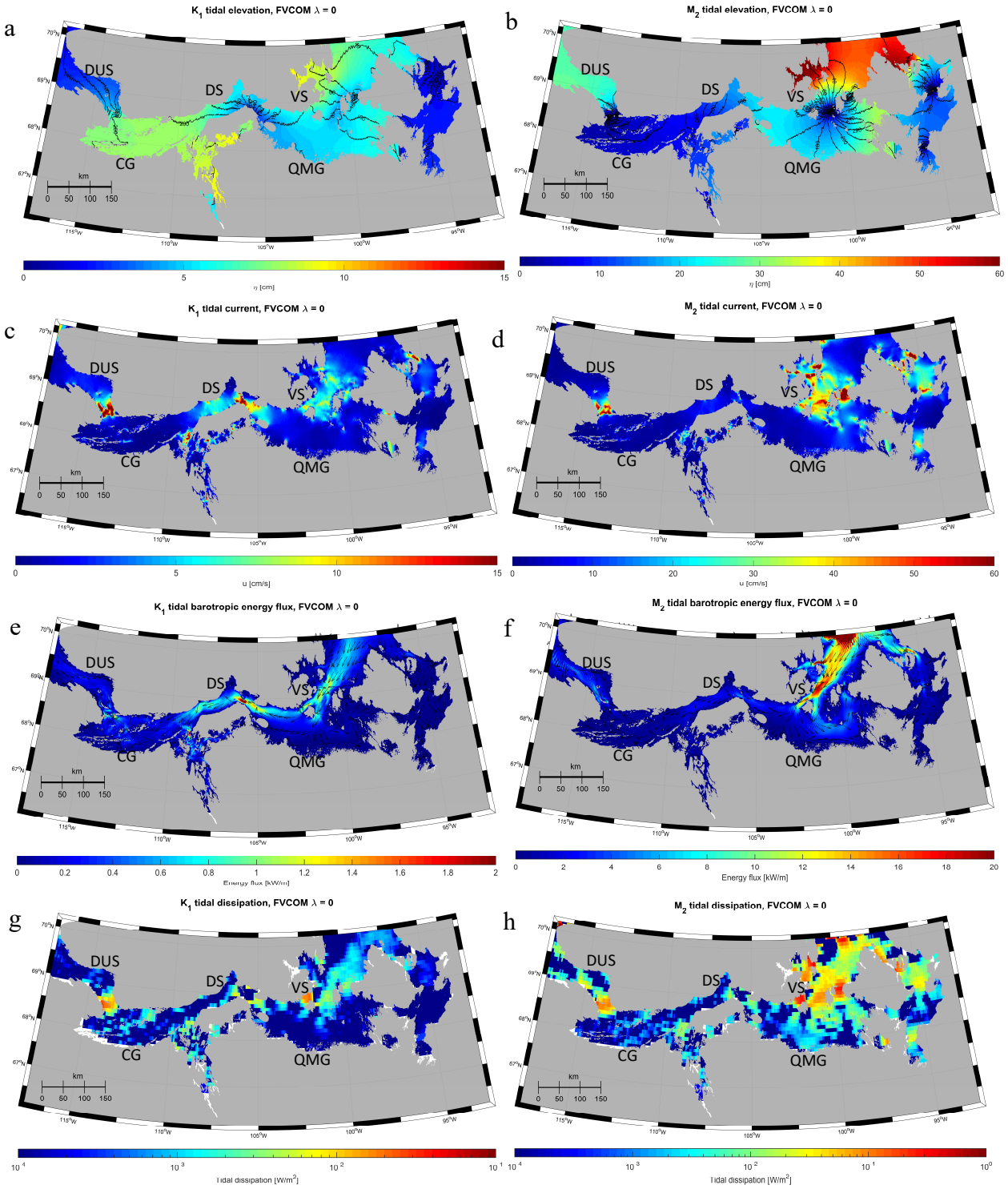

Figure 10. Tidal charts for the FVCOM simulation A, $\lambda = 0$ m^{-1} (no sea ice). (a, b) Tidal elevation, (c, d) tidal currents, (e, f) average energy flux and (g, h) tidal dissipation for the K_1 and M_2 tides, respectively. (a, b) The black lines are elevation phase [°] contours in 10° intervals. (e, f) Magnitudes of energy flux are indicated by the contour color, and direction by the arrows. For all plots, the K_1 and M_2 tides are scaled separately.

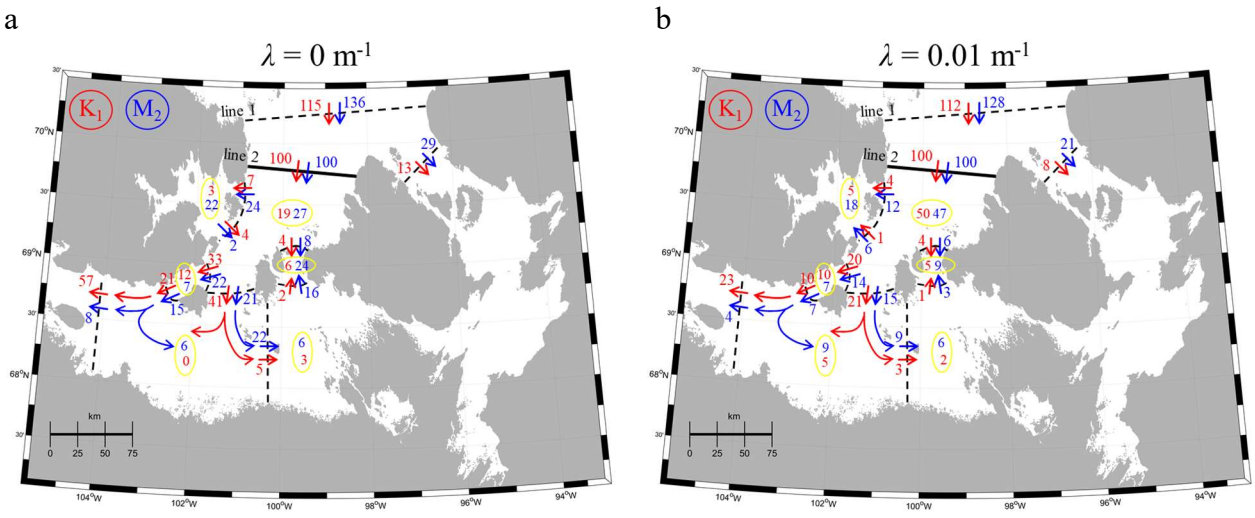

Figure 11. Estimates of the change of energy flux (%) through eastern Kitikmeot Sea for (a) simulation A (λ = 0 m^{-1}) and (b) simulation D (λ = 0.01 m^{-1}). Red correspond to the K_1 tide, and the blue values correspond to the M_2 tide. Estimates of tidal dissipation (%) are circled in yellow. All values are normalized with respect to line 2 values. Arrows are not to scale.

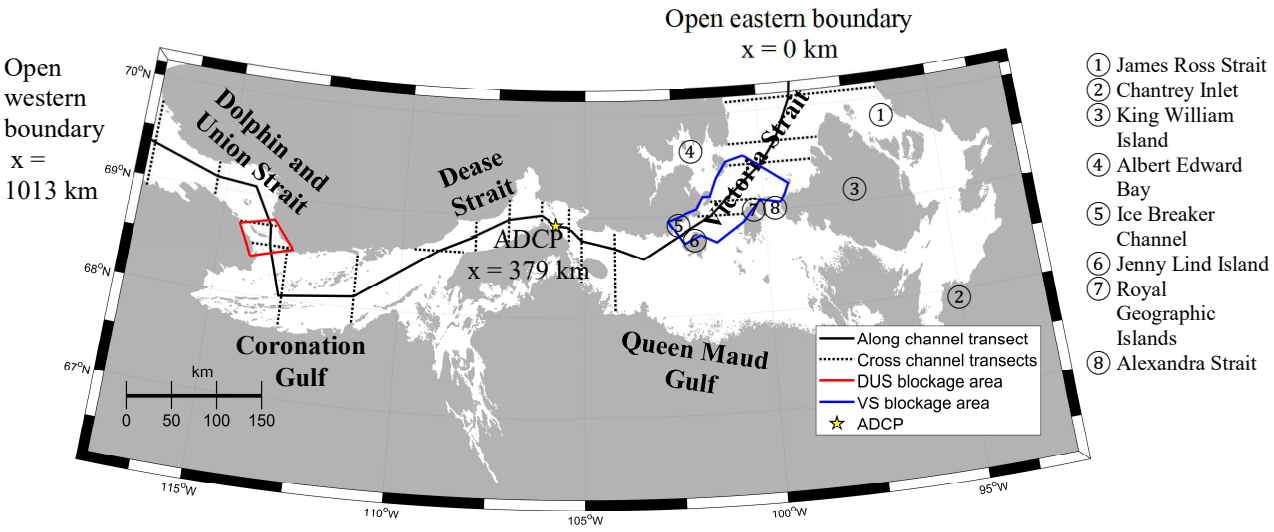

Figure 12. The black line is the along transect location for the Kitikmeot Sea. Along this distance tidal elevation and current amplitudes and phases are plotted (Figure 14). Along this distance, at each cross transect (black dotted lines) the total energy flux across the channel was calculated (Figure 13 and Figure 15).

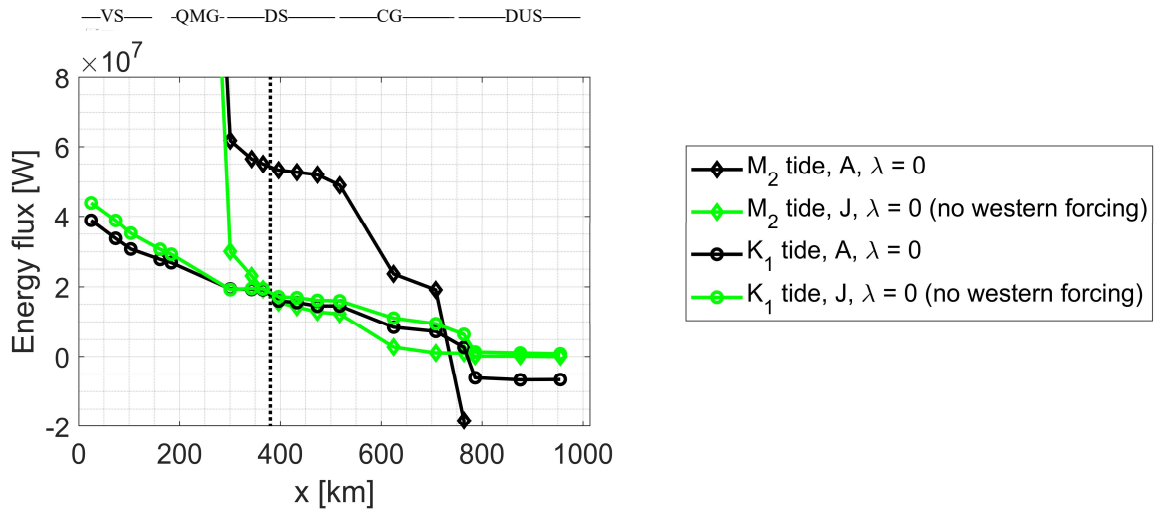

Figure 13. Comparing the M_2 and K_1 tidal energy flux [W] in simulations A ($\lambda = 0$ m^{-1}) and J ($\lambda = 0$ m^{-1}, no western forcing). The energy flux is integrated over the cross channel transects for the along transect within the Kitikmeot Sea. x = 0 km is the eastern side. Positive energy flux in the direction of increasing *x* along the transect.

The K_1 tide in the Kitikmeot Sea, particularly DS, is influenced primarily by eastern K_1 tidal forcing entering through VS, while the western K_1 tidal forcing entering through DUS is negligible (Figure 10 – 13). The K_1 energy flux entering VS is approximately 3.4×10^7 W and propagates far into the Kitikmeot Sea with 57% of the K_1 tide entering VS reaching DS (Figure 10e and Figure 11a). Of the energy flux entering VS, only 3% is diverted into Albert Edward Bay and 4% into Alexandra Strait, and 19% is dissipated within VS. The K_1 energy flux in VS is further split into two branches by Jenny Lind Island as is propagates into QMG. The western branch propagates through Ice Breaker Channel where 12% is dissipated. The majority of the eastern branch rejoins the western branch propagating towards DS, and only 5% propagates into eastern QMG, some of which continues into Alexandra Strait where tidal energy is entering from both sides. A total of 6% of the energy flux entering VS is dissipated in Alexandra Strait and 3% in eastern QMG. About 57% of the energy flux entering VS reaches DS, the rest is dissipated within VS region and in adjoining bays and straits (Figure 10g and Figure 11a). Areas of large dissipation correspond with areas of large velocity (Figure 10c). Within DS and CG the K_1 tide behaves as a Helmholtz resonator (see section 3.3 for more details). The following tidal features within DS are

similar to that of the channel response for a Helmholtz resonator. Within DS a tidal elevation minimum occurs before amplifying towards CG (Figure 10a). Additionally, the phase shifts 110° across DS and then remains roughly constant within CG (Figure 10a). The K_1 tide entering CG through DUS is negligible (Figure 13, black vs green line). Comparing the K_1 tidal energy flux of simulation A ($\lambda = 0$) with simulation J ($\lambda = 0$, no western Arctic tidal forcing) shows that removing western forcing from the model does not significantly change the K_1 energy flux within the Kitikmeot Sea.

The M_2 tide in the Kitikmeot Sea, particularly DS, is partially influenced by western M_2 tidal forcing and is dominated by the eastern tidal forcing. The M_2 energy flux entering VS is approximately 7.4×10^8 W, much larger than the K_1 energy flux, however, unlike the K_1 tide, does not propagate far into the Kitikmeot Sea (Figures 10 – 13). Of the tidal energy flux entering VS only 8% reaches DS. For the M_2 tide, with half the wavelength of the K_1 tide, more semidiurnal energy propagates into adjoining bays and counter clockwise around an amphidromic point west of King William Island (Figure 10b). Of the energy flux entering VS, 22% of it is diverted into Albert Edward Bay and 8% into Alexandra Strait, and 27% is dissipated in VS. Within VS the tidal energy is split by Jenny Lind Island into two paths; the western path propagating towards DS and the eastern path following the counter clockwise rotation around the amphidromic point. As the western branch propagates through Ice Breaker Channel 7% is dissipated. The western path then splits into two more branches, one path propagating towards DS and the other following the counter clockwise rotation around the amphidromic point and rejoining the eastern path towards eastern QMG. Of the initial energy entering VS, 22% propagates into eastern QMG some of which continues into Alexandra Strait where tidal energy is entering from both sides. A total 24% of the energy flux entering VS is dissipated in Alexandra Strait and 6% in all of eastern QMG. Of the initial energy entering VS, only 8% reaches DS, as a significant portion is dissipated within Albert Edward Bay, Alexandra Strait, VS, Ice Breaker Channel and eastern QMG (Figure 10h and Figure

11a). The dissipation corresponds with areas of large velocity (Figure 10d). By the time it reaches CG, the M_2 tidal elevation averages 1.5 smaller than the K_1 tidal elevation (Figure 10b). The M_2 tidal elevation in CG, DS and QMG is also influenced by western M_2 tidal forcing. Omitting western tidal forcing alters the M_2 energy flux significantly (Figure 13), showing that the western Arctic tidal forcing is not negligible for the M_2 tide.

3.2.2 FVCOM results with sea ice friction ($\lambda \neq 0$ m^{-1}) and sea ice ridging

K_1 and M_2 tidal features, previously mentioned, are similarly shown along the transects of amplitudes and phases throughout the Kitikmeot Sea (Figure 14 and Figure 15). The features can be compared to FVCOM simulations B – I which model various conditions of sea ice roughness and ridging.

The M_2 and K_1 tidal elevation and currents are systematically reduced with increasing values of the sea ice friction, (Figure 14, simulations B – F). Simulations B – F (Table 1) used increasing values of sea ice friction, λ = 0.002, 0.004, 0.01, 0.02 and 0.03 m^{-1}, with an affected depth of 1 m. Simulation E1 had a sea ice friction value of λ = 0.02 m^{-1}, with an affected depth of 2 m. Amplitudes are reduced not only by increasing the ice-ocean drag coefficient, but also by increasing the depth to which the water column is affected by sea ice (comparing simulation E and E1). The K_1 elevation phase shifts positive throughout most of the Queen Maud Gulf to Coronation Gulf region, while the M_2 elevation phase shifts negative (Figure 14), as observed within Dease Strait from the ADCP data. No systematic current phase changes occurred. Energy flux along the Queen Maud Gulf to Coronation Gulf region is also reduced with increasing sea ice friction (Figure 15). The primary increase of tidal dissipation during sea ice cover is within VS increases. Within VS, the K_1 tide dissipates 19% and the M_2 tide 27% during ice free periods (simulation A, λ = 0 m^{-1}); this percentage increases to 50% and 47% with sea ice cover (simulation D, λ = 0.01 m^{-1}) for the K_1 and M_2 tides, respectively (Figure 11b).

Sea ice blockages augment the effects that sea ice friction has on amplitudes within the region close to the blockage, but does not greatly affect the amplitudes in regions very far away from the blockage. Simulations G – I (Table 1) have a background sea ice of $\lambda = 0.01$ m^{-1}, affecting the water column to a depth of 1 m. Simulations G and H (red lines) included sea ice blockages in VS of 5.4 m and 12 m thick, respectively and simulation I (blue line) included a DUS blockage. Each element in the blockage has a drag coefficient $\lambda = 0.6$ m^{-1}. The DUS blockage affects the western regions, generally reducing tidal elevation and currents from DUS to western Dease Strait (Figure 14), and not affecting the eastern side. VS blockages significantly reduce the elevation and current amplitudes on the eastern side of the Kitikmeot Sea until western Dease Strait (Figure 14). With a sea ice blockage in VS (simulation G) even less energy flux reaches DS, 10% and 2% for the K_1 and M_2 tides, respectively. Blockages in VS also increase the tidal dissipation even further within VS; for simulation G (5.4 m VS blockage) the percentage tidal dissipation in VS increases to 69% and 65% for the K_1 and M_2 tides, respectively. Dissipation in VS is roughly doubled during wintertime ice cover due to friction at the ice-ocean interface and sea ice blockages, so within the Kitikmeot Sea the wintertime damping of the tides is likely due to sea ice friction and tidal-induced, sea ice ridging in Victoria Strait.

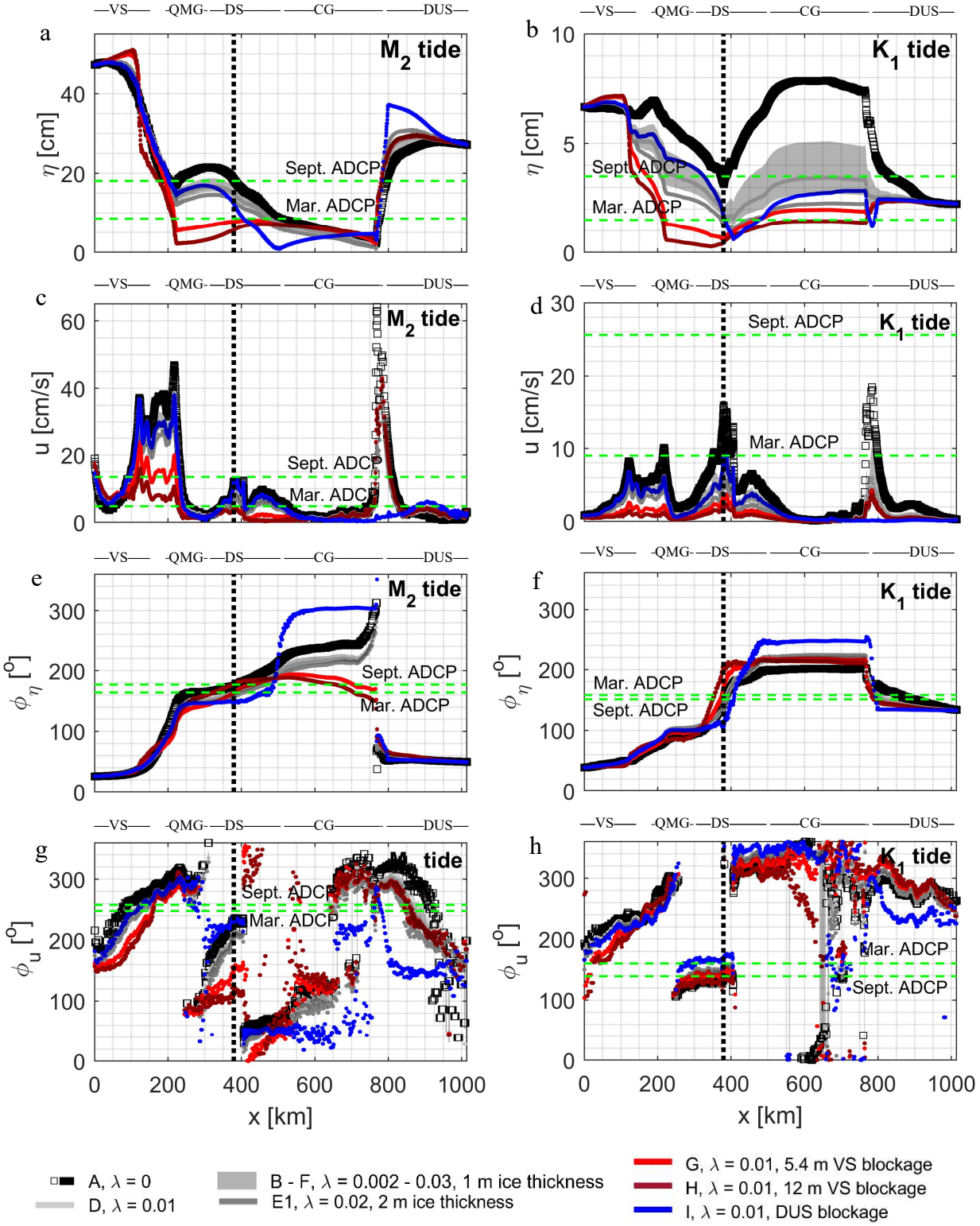

Figure 14. M_2, K_1 tidal elevation (a, b) amplitude and (e, f) phase and M_2, K_1 tidal current (c, d) amplitude and (g, h) phase, along a transect in the Kitikmeot Sea. x = 0 km is the eastern open boundary, while x ≈ 1013 km is the western open boundary. Dotted black line indicated the ADCP location. Green dashed lines indicate Sept. or Mar. ADCP observations. (g, h) Artificial 180° phase jumps occur because the inclination angle is restricted between 0° - 180° (Pawlowicz et al., 2002).

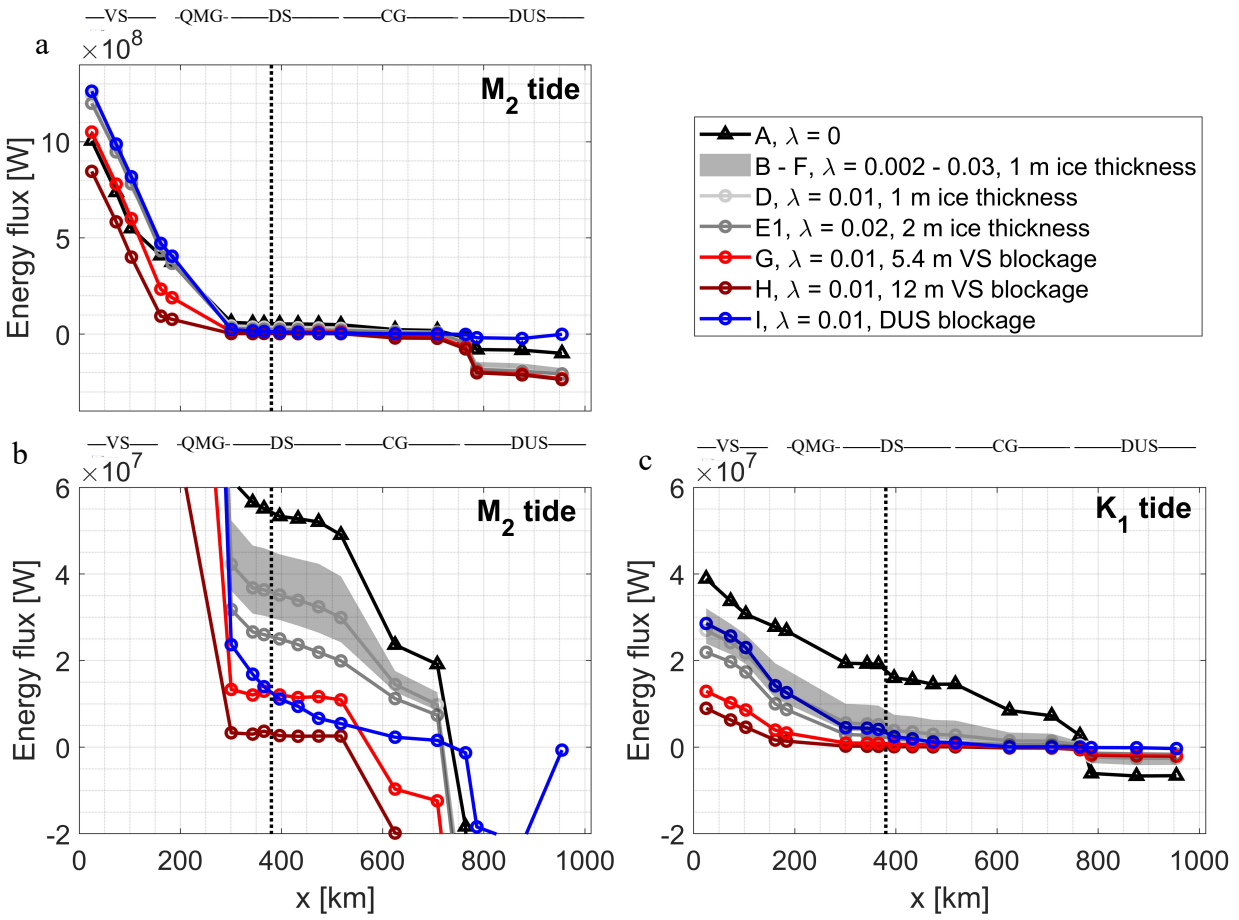

Figure 15. Energy flux [W] integrated over the cross channel transects for the (a, b) M_2 tide and (c) K_1 tide along transect within the Kitikmeot Sea. x = 0 km is the eastern side of the model. Panels (b) and (c) and on the same scale. Positive energy flux in the direction of increasing *x* along the transect.

For the K_1 tide, the best simulations are the ones with very high λ values (simulations F and E1, Table 4). The dampening of the observational K_1 tidal elevation and current best matches simulations F and E1. The observational phase of the K_1 tidal elevation did not show a clear seasonal pattern. The phase shift in simulations F and E1 is in the wrong direction compared to March observations for the K_1 tidal elevation, but does match January observations. Introducing the VS blockage shifts the phase in the correct direction compared to March observations. For simulations F and E1, the phase shift for the K_1 currents is in the correct direction, however the shift is 10° to small compared to observations.

Simulations G, which includes a Victoria Strait blockage, best matches observed changes in the M_2 tides (Table 4). Simulations without this blockage does not result in the observed

dramatic decrease in M_2 tidal elevation and currents. All phase shifts are in the correct direction compared to the M_2 tidal observations. The phase shift for elevation is within 2° of observations for simulation G, but the phase shift in the tidal currents is larger than observations by 70°. High values of sea ice drag or sea ice blockages in Victoria Strait need to be included in the FVCOM model in order to reproduce observed seasonal changes in the ADCP data and correctly predict seasonal tidal variability.

Table 4. All elevation and current amplitudes and their phases at the mooring location during ice-free conditions (harmonic analysis of the ADCP centered around the date 01-Sept-2016, and data from the models WebTide and FVCOM simulation A with $\lambda = 0$ m^{-1}) and ice covered conditions harmonic analysis of the ADCP centered around the date 06-Mar-2017, and FVCOM simulations B – I with $\lambda \neq 0$ m^{-1}).

Description			λ [m^{-1}]	h [m]	M_2				K_1			
					η [cm]	φ_η [°]	u [cm/s]	φ_u [°]	η [cm]	φ_η [°]	u [cm/s]	φ_u [°]
Ice-free period	ADCP, 01-Sept-2016		-	-	18.1	177	13.5	258	3.5	151	25.6	139
	WebTide		-	-	9.0	170	7.1	208	7.2	105	24.6	104
	FVCOM simulation A		0	0	18.3	175	11.3	233	3.4	151	14.6	142
Ice-covered period	ADCP, 06-Mar-2017		-	-	8.6	164	4.8	248	1.5	158	9.0	160
	FVCOM simulations	B	0.002	1	16.3	167	9.8	218	2.2	146	10.6	148
		C	0.004	1	15.6	165	9.3	214	2.0	144	9.3	150
		D	0.01	1	14.6	161	8.6	210	1.7	142	7.7	152
		E	0.02	1	14.0	160	8.1	207	1.5	141	6.7	153
		F	0.03	1	13.6	159	7.9	206	1.4	140	6.3	153
		E1	0.02	2	12.9	157	7.3	205	1.3	140	5.2	153
		G	0.01	1 m + 5.4 m VS blockage	7.7	164	4.3	153	0.7	174	3.6	146
		H	0.01	1 m + 12 m VS blockage	5.7	179	4.0	115	0.5	202	2.3	135
		I	0.01	1 m + DUS blockage	12.1	148	12.1	233	1.7	114	8.4	170

3.3 Analytical model – the Helmholtz resonator

Coronation Gulf and Dease Strait act as a simple Helmholtz resonator for diurnal frequencies. Tides in coastal basins, inlets, channels, can be amplified dependent on the geometry

of the basin and its natural frequencies. The Helmholtz resonator (Leblond and Mysak, 1978; Lee, 1971; Platzman, 1972; Miles and Lee, 1975) consists of an inner basin (Coronation Gulf), connected via a narrow constriction or channel (Dease Strait) to the greater ocean (Queen Maud Gulf/ eastern Kitikmeot Sea) (Figure 16). Dolphin and Union Strait is neglected. The simplified geometry is depicted in the schematic Figure 16, where A_b is the area of the basin, $A_c = LW$ is the area of the channel, L is the length of the channel, W is the width of the channel, and H is the depth of the channel.

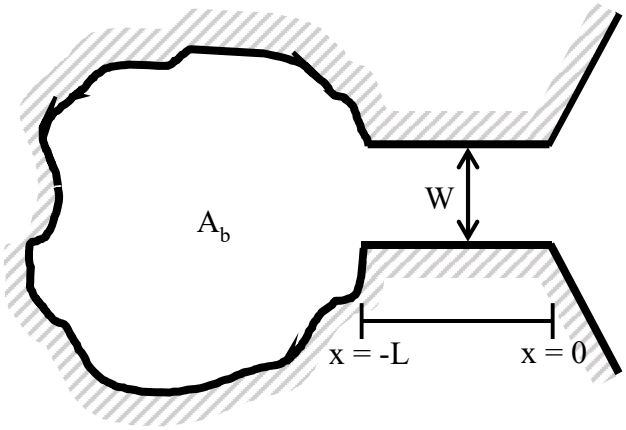

Figure 16. Schematic of a Helmholtz resonator. A_b is the area of the inner basin, W is the channel width and L is the length of the channel.

This simple model is adapted from Cummins et al. (2010) (equations 1 – 10 in Cummins et al. 2010). The average channel width is narrow compared to the Rossby radius (185 km), so Coriolis effects are neglected making the currents within the channel uniform across its width. The channel is also approximated to be of constant width (25 km) and depth (64 m). The 1D linear shallow water momentum and continuity equation are, respectively:

$$\frac{\partial u}{\partial t} = -g\frac{\partial \eta}{\partial x} - ru \qquad (5)$$

$$\frac{\partial \eta}{\partial t} + H\frac{\partial u}{\partial x} = 0 \qquad (6)$$

Here water elevation and velocity are $(\eta(x,t), u(x,t)) = [\tilde{\eta}(x), \tilde{u}(x)]e^{i\omega t}$ and g is gravity, t is time, x is the along channel distance. The linear drag coefficient is $r = \frac{C_D|U|}{H}$, where C_D is the drag

coefficient and $|U|$ is the scale tidal speed. Inputting the $\eta(x,t)$ and $u(x,t)$ into equations 5 and 6 simplifies them to:

$$i\omega\tilde{u} = -g\frac{d\tilde{\eta}}{dx} - r\tilde{u} \tag{7}$$

$$i\omega\tilde{\eta} + H\frac{d\tilde{u}}{dx} = 0 \tag{8}$$

Combining equations 7 and 8 yields,

$$\frac{\partial^2\tilde{\eta}}{\partial x^2} + k^2\tilde{\eta} = 0 \tag{9}$$

Here $k^2 = k_o^2(1 - \mathrm{i}\,\delta)$ is the complex wavenumber where $k_o = \frac{\omega}{\sqrt{gH}}$ and $\delta = \frac{r}{\omega}$. The boundary condition for the channel at x = 0 is:

$$\tilde{\eta}(0) = \eta_o \tag{10}$$

and volume conservation leads to the boundary condition for the channel basin junction at x = – L:

$$i\omega\tilde{\eta}_b = \frac{WH}{A_b}\tilde{u}(-L) \tag{11}$$

$$\tilde{\eta}_b = \alpha\tilde{\eta}(-L) \tag{12}$$

$\tilde{\eta}_b$ is the basin averaged elevation amplitude and α is a complex constant. Manipulating equations 7, 11, and 12 leads to a modified boundary condition at x = – L:

$$\frac{d\tilde{\eta}}{dx} = -\frac{\alpha}{\gamma}k^2L\tilde{\eta} \qquad \text{where,} \qquad \gamma = \frac{A_c}{A_b} \tag{13}$$

Using $\tilde{\eta} = Acos(kx) + Bsin(kx)$ and applying the boundary conditions to equations 9 and 7 yields:

$$\tilde{\eta}(x) = \eta_o\left(cos(kx) - \frac{sin(kL)+\frac{\alpha kL}{\gamma}cos(kL)}{cos(kL)-\frac{\alpha kL}{\gamma}sin(kL)}sin(kx)\right) \tag{14}$$

$$\tilde{u}(x) = -i\eta_o F(\delta)\sqrt{\frac{g}{H}}\left(sin(kx) + \frac{sin(kL)+\frac{\alpha kL}{\gamma}cos(kL)}{cos(kL)-\frac{\alpha kL}{\gamma}sin(kL)}cos(kx)\right) \tag{15}$$

$$F(\delta) = \frac{2+\delta^2+i\delta}{2(1+\delta^2)} \quad (16)$$

Finally, water elevation and velocity amplitude and phase are:

$$u(x,t) = |\tilde{u}|\cos(\omega t - \varphi_u) \qquad \varphi_u(x) = -atan2(Im(\tilde{u}), Re(\tilde{u})) \quad (17)$$

$$\eta(x,t) = |\tilde{\eta}|\cos(\omega t - \varphi_\eta) \qquad \varphi_\eta(x) = -atan2(Im(\tilde{\eta}), Re(\tilde{\eta})) \quad (18)$$

The tidal elevation and currents depend on the basin geometry α/γ and k_oL and the bottom friction δ. For now, channel friction is neglected, setting $F(\delta) = 1$ and $k^2 = k_o^2$. The Helmholtz resonator requires that the phase remains constant within the inner basin; this is approximately true for CG. Assuming low frequency forcing ($k_oL << 1$), the basin water elevation responds in phase with the channel end, making α a real constant that can be set to 1 without loss of generality. When $\alpha = 1$ there is no energy flux into the basin, hence the phases of water elevation and currents are in quadrature at the channel basin junction. Resonance occurs when the impedance is at a minimum (Cummins et al., 2010): $|Z(0)| = \left|\frac{\rho g}{WH}\frac{\tilde{\eta}(0)}{\tilde{u}(0)}\right| = 0$, which is when $\frac{k_o^2L^2}{\gamma} = 1$ or, rearranged, the Helmholtz frequency is (Mullarney et al. 2008; Cummins et al. 2010):

$$\omega_h = \sqrt{\frac{gHW}{A_bL}} = \frac{\sqrt{gH\gamma}}{L} \quad \rightarrow \quad T_h = \frac{2\pi}{\omega_h} = \frac{2\pi L}{\sqrt{gH\gamma}} \quad (19)$$

For the geometry of Coronation Gulf and Dease Strait, the Helmholtz period is T_h = 27.0 h (without friction), which is three hours longer than the period of diurnal tides; K_1 has a period of 23.9 h. Constraining the location of where the channel begins amounts to uncertainties of the Helmholtz period. The basin area, A_b, is 18.8 × 10^9 m^2 and channel depth was assumed constant at H = 64 m. The area and length of the channel is A_c = 5.0 × 10^9 m^2 and L = 200 km. The effects of bottom friction lead to decrease (increase) the Helmholtz frequency (period) (Mullarney et al. 2008; Cummins et al. 2010). The linear drag coefficient is $r = \frac{C_D|U|}{H}$, where C_D the friction coefficient is a combination of bottom friction and surface friction due to sea ice. For the ice-free

conditions, $C_D = C_{D,bottom} = 0.0025$ and in the ice-cover conditions $C_D = C_{D,bottom} + C_{D,ice} = 0.0025 + 0.02$. U was set to 0.5 m/s and 0.2 m/s, for ice-free and ice-cover conditions respectively. The linear drag coefficient is then scaled by $\omega = 7.3 \times 10^5$ s^{-1} (K_1 frequency), so δ=r/ ω. This resulted in $\delta = 0.3$ and $\delta = 1.0$ for ice-free and ice-cover conditions respectively. Multiple resonant peaks are visible for the idealized model (Figure 17), the first peak at $k_oL = 0.459$ (black, $\delta = 0.3$) and 0.311 (blue, $\delta = 1.0$). These values lead to a Helmholtz period of $T_h = 30.4$ and 44.9 h with friction $\delta = 0.3$ and 1.0. The other peaks correspond to resonant periods of 9 h or less.

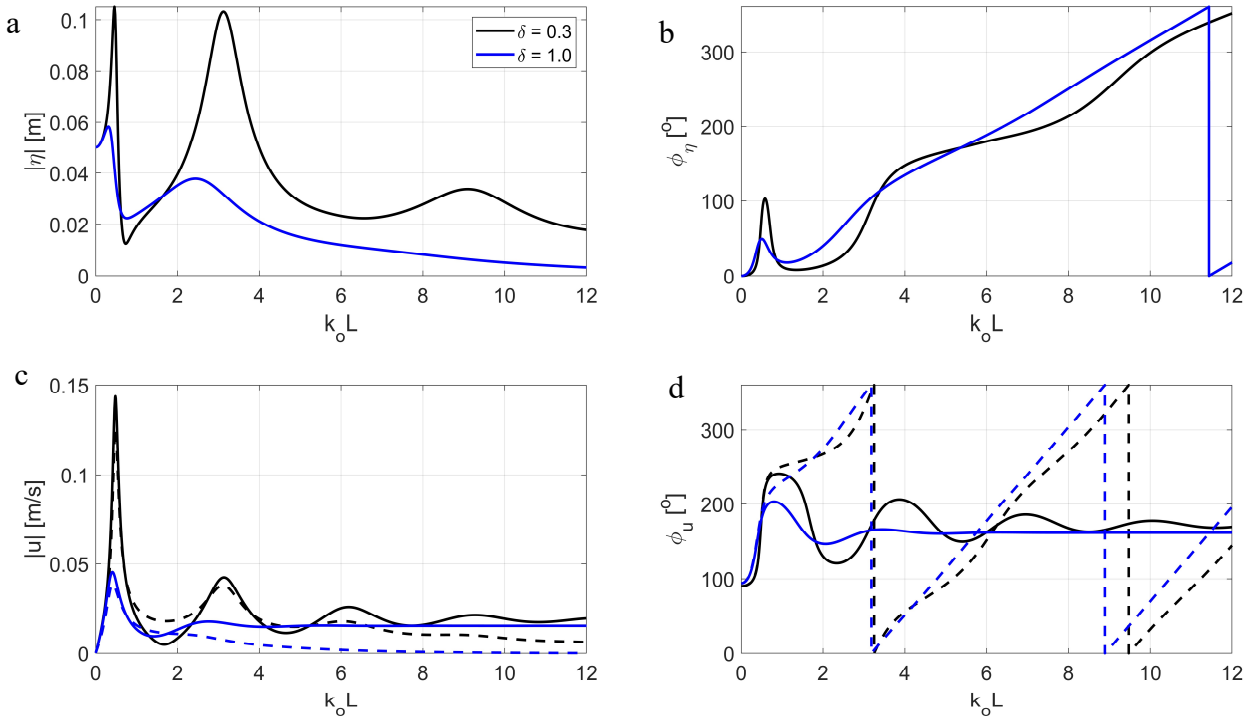

Figure 17. Amplitude and phase of (a, b) elevation at $x = -0.5L$ and (c, d) velocity at $x = 0$ (solid) and $x = -L$ (dashed) as a function of k_oL for the analytical model (equations 14 and 15). Parameters used: $\eta_o = 5$ cm, $A_c = 5.0 \times 10^9$ m^2, $L = 200$ km, $A_b = 18.8 \times 10^9$ m^2, $\alpha = 1$, $\delta = 0.3$ (black) and $\delta = 1.0$ (blue).

The channel response for a Helmholtz resonator model is similar to the channel response of the FVCOM simulations within Dease Strait at diurnal frequencies (Figure 18, comparing red lines to dotted black/gray lines). In both models the water elevation amplitude initially decreases at the beginning of the channel and then begins to rise again around the ADCP location, however at slightly different rates. Increasing channel friction drastically reduces the amplitude increase,

because when friction increases the resonant Helmholtz period moves further away from diurnal frequencies. With δ = 0.3 the amplitude minimum is 2.5 cm and increases to 9 cm by the end of the channel (Figure 18, solid red line), while for the δ = 1.0 the amplitude minimum is 1 cm and only increases to 1.6 cm (Figure 18, dashed red line). The amplitude minimum also extends further down the channel with higher values of friction. In both models the phase of water elevation shifts by about 110° over the channel length, and the phase of currents remains approximately constant. With increasing friction the phase increase seen along the channel becomes marginally smaller and the shift does not occur as rapidly (Figure 18, dashed red line). For the Helmholtz resonator, the channel response of the velocity amplitude and phase remains fairly constant at 8.5 cm/s and 1.5 cm/s respectively for the δ values of 0.3 and 1.0, and 320° and 300° respectively for the δ values of 0.3 and 1.0 (Figure 18, solid and dashed red lines). In the FVCOM simulations currents do not remain constant, because the FVCOM includes a constriction at the Finlayson Islands, unlike the analytical Helmholtz model.

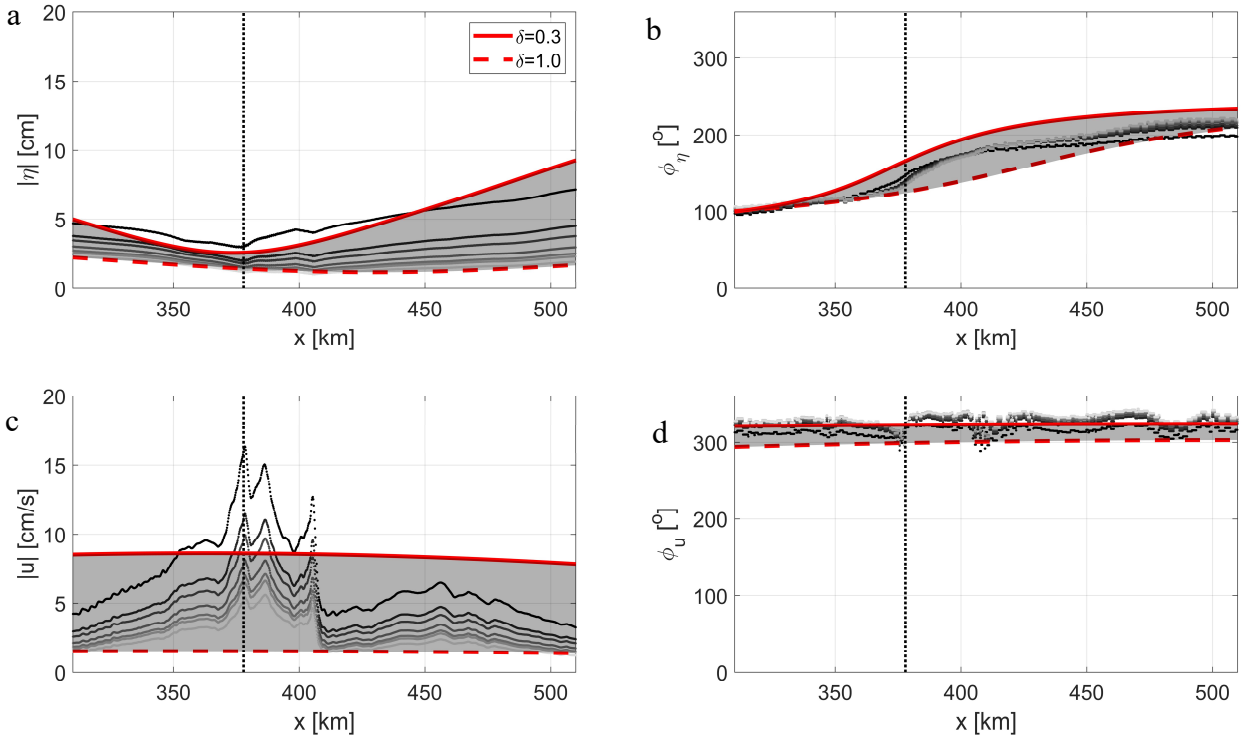

Figure 18. Amplitude and phase of (a, b) elevation and (c, d) velocity along channel distance x, where x = 310 km is the channel mouth and x = 510 km is the channel basin junction. Red lines are the analytical model (equations 14 and 15). Parameters used: $k_oL = 0.582$, $\eta_o = 5$ cm (ice-free) and $\eta_o = 2.3$ cm (ice-covered), $A_c = 5 \times 10^9$ m^2, $L = 200$ km, $A_b = 18.8 \times 10^9$ m^2, $\alpha = 1$, $\delta = 0.3$ (red solid, ice-free) and $\delta = 1.0$ (red dashed, ice-covered). The dotted black – to gray are the responses of FVCOM simulations A - F.

The Helmholtz resonator is an idealized analytical model; despite the many assumptions made it describes diurnal frequencies in the Coronation Gulf and Dease Strait system well. The analytical model assumes a channel of constant width and depth, which in reality it is not, varying these parameters could influence the channel response. In the FVCOM simulations the elevation and current is not uniform across the channel's width as assumed by the analytical model. This analytical model works because western Arctic influences are negligible for the K_1 tide, the same cannot be stated about the semidiurnal frequencies for which the western Arctic tide has a significant impact on the M_2 tides in Coronation Gulf. The period of the M_2 tide is not resonant within the CG and DS geometry. Additionally, at the M_2 frequency Coronation Gulf does not respond in phase with the channel end, a criteria for the Helmholtz resonator.

4. Discussion and summary

4.1 Examining the greater CAA

This paper's FVCOM model, as well as in-situ observations, are limited to the Kitikmeot Sea, but is the Kitikmeot Sea unique or does sea ice impact the tide throughout the CAA? We looked at the seasonality of the tides using the Canadian tides and water level data back to 1967 from Fisheries and Oceans Canada (Isdm-gdsi.gc.ca, 2019). Spatial variations in the strength of the tidal seasonality within the CAA show that the seasonal reduction of the tides (% relative to ice-free conditions) is strongest within the Kitikmeot Sea. The 1.5 monthly harmonic analysis used in section 3.1.2 was applied to each station with a minimum of about an eight month time record (Figure 19). In the Kitikmeot Sea the ice-cover M_2 tidal amplitude are reduced by 40 – 50% relative to ice-free M_2 tidal amplitude (Figure 19). In the western CAA, the M_2 tidal amplitude is moderately reduced by 20 – 30% seasonally, while in the rest of the CAA the tides are only damped 0 – 10% seasonally. This analysis indicates that greater tidal damping due to sea ice occurs within the Kitikmeot Sea. Within the region, frictional decay of the tides is increased over the shallow sills of DUS and VS, which is then further amplified with the addition of sea ice cover and sea ice blockages.

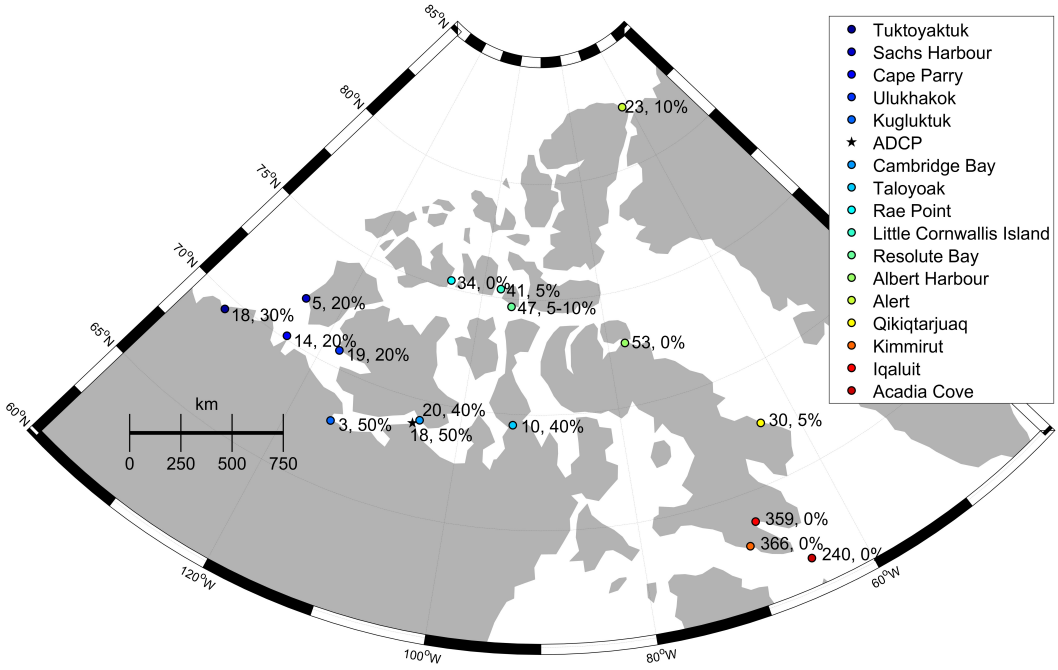

Figure 19. Seasonal reduction of the M_2 tidal amplitude within the CAA is strongest within the Kitikmeot Sea. The first value is the maximum M_2 tidal amplitude [cm] (ice-free conditions), and the second value is the amount the M_2 tide has been damped in% relative to ice-free conditions. Data obtained from Canadian tides and water level data from Fisheries and Oceans Canada.

4.2 Limitations and future research

Higher spatial resolution in observations would allow us to improve our model validation. In this paper, model validation was limited to a one year-long mooring deployment, which was located close to a constriction where the currents vary drastically spatially. Furthermore, the phase of K_1 tidal elevation rapidly changes through Dease Strait. Additional moorings in regions where the currents and phases vary slowly spatially would be helpful in validating the model and differentiating the relative importance of high sea ice friction and a sea ice blockage in Victoria Strait. Potential locations of these new moorings could be one on either side of Dease Strait, in western Queen Maud Gulf and eastern Coronation Gulf. Moorings in the location of the Victoria Strait blockage would be of great interest too. Victoria Strait has moderate dissipation in ice free periods, but is modelled to approximately double in tidal dissipation during ice covered periods. Attaining in-situ measurements from these locations would be very useful in understanding tidal dissipation within the area.

This study focused on barotropic tides, and assumed baroclinic tides were negligible. Further research would include stratification in FVCOM to study the baroclinic tides as well. In September there is strong stratification, but during the ice-covered periods the stratification reduces to zero.

The sea ice in our model is simulated by implementing a body force on certain elements within the water column, it is not a coupled sea ice model that implements a surface boundary drag. In our model the upper vertical grid size varies, which in turn leads to a varying sea ice depth, so having our model account for partial grid cell depths could improve the model. Other ways to improve the model is to have λ or $g(z)$ vary spatially, and temporally, so we could implement a combination of smooth land-fast ice and mobile deformed sea ice, this would produce a time varying sea surface drag.

Implementation of the sea ice blockages is a unique feature of our model that allows us to better understand sea ice ridging and its effects on the tides. In the location of the sea ice blockages, tidal flow is reduced. Dampened tidal flows could lead to less sea ice mobility and therefore potentially less sea ice ridging occurs in the southern part of the Strait. A variety of sea ice blockages still need to be tested. Simulations combining high levels of sea ice friction with thinner ridges should be implemented, as our results suggest that both high sea ice friction and sea ice blockages could produce our observed changes. Additionally, blockages placed only in small spatial regions affect the M_2 and K_1 tides differently. The tides dissipate differently in some of the channels; for example a blockage in Alexandra Strait might significantly affect the M_2 tide but not the K_1 tide.

4.3 Summary

Sea ice impacts the tides in the Kitikmeot Sea, and tides and tidal mixing are also known to impact sea ice formation and mobility, heat and nutrient fluxes throughout the Arctic. Enhanced

tidal mixing in narrow and shallow constrictions leads to elevated nutrient fluxes and ecosystem hotspots. As sea ice is declining in the Arctic, longer ice-free seasons will lead to longer periods of strengthened tides, which will then have impacts on vertical mixing, primary production and polynya formation. It is therefore important to understand the link between sea ice and tides, particularly where this link is the strongest. Past studies have found sea ice influences on tides in Hudson Bay System and the Siberian Continental Shelf as well in western parts of the CAA. However, seasonality of the tides had not yet been studied in the Kitikmeot Sea, where the influence of sea ice on the tides is strong. In addition, we highlight the importance of a likely sea ice blockage in Victoria Strait and its impact on the tides.

The dynamics of the Kitikmeot Sea are complex: Atlantic tides enter from the east, through Victoria Strait, and these dominate over the Arctic tides that enter from the west, through Dolphin and Union Strait. Although secondary, the Arctic M_2 tide has a significant impact in Coronation Gulf, while the Arctic K_1 tide is negligible. The M_2 and K_1 tides have different behaviours in the Kitikmeot Sea: K_1 tidal dynamics can be modelled with a Helmholtz resonator in which the Coronation Gulf (inner basin) / Dease Strait (channel) system amplifies the K_1 tidal elevation in the inner basin comparatively to Queen Maud Gulf (Figure 18). An elevation phase shift of 110° in Dease Strait is seen in both this idealized model and FVCOM simulations. The K_1 energy flux entering the eastern model domain propagates far into the Kitikmeot Sea, with 57% of initial K_1 tidal energy reaching Dease Strait (Figure 11a). This is because the K_1 tide, with double the wavelength of the M_2 tide, does not get significantly diverted into the smaller adjoining bays, inlets, gulfs and straits.

In contrast, the M_2 tide cannot be modelled using a simple Helmholtz resonator because the M_2 tide is influenced by both Arctic and Atlantic tides and the M_2 frequency is much higher than the Helmholtz frequency for the geometry of Coronation Gulf and Dease Strait. The M_2 tide's wavelength is short enough that it does get significantly diverted into, and dissipated in, adjoining

bays and gulfs. The most striking of these diversions is an amphidromic point that forms west of the King William Island, which drives about 26% of the tide anticlockwise into eastern Queen Maud Gulf which then predominately dissipates in Alexandra Strait (Figure 10). Similar portions of the M_2 tide are diverted to neighbouring Albert Edward Bay and James Ross Strait and dissipate there. In addition, 27% of M_2 tidal energy dissipates directly within Victoria Strait, so only 8% of M_2 energy that enters Victoria Strait reaches Dease Strait (Figure 11a).

This paper shows that the seasonal modulation of the tides in the Kitikmeot Sea is likely due to extremely rough sea ice and ridging in Victoria Strait. From ice-free periods to conditions of maximum ice cover, the M_2 and K_1 observed tidal elevation and current amplitudes decrease 52 – 65% (Figures 8 and 9). The phase of the M_2 elevation and current shifts seasonally by -13° and -10°, respectively, and the K_1 current phase by +21°. The variability of the K_1 elevation phase is masked by its large uncertainties. In both analytical and numerical models, increased friction damps tidal amplitudes, and the addition of a blockage in Victoria Strait further reduces amplitudes in the numerical model. FVCOM simulations with high ice-ocean drag coefficient (simulations E1: λ = 0.02 m^{-1} to 2 m and F: λ = 0.03 m^{-1} to 1 m) and a sea ice blockage in Victoria Strait (simulations G: 5.4 m blockage) match the observed seasonal changes in the tides (Table 4). For the M_2 tide, sea ice friction alone is not enough to model the observed changes in the tide, a blockage is required in Victoria Strait. Blockages in Victoria Strait roughly double the amount of dissipation that occurs in the Victoria Strait, dampening the tides. Victoria Strait is a likely location for a blockage because this region remains mobile longer into the winter months leading to ridging and thicker sea ice (Figure 3 and 4). For the K_1 tide, high values of sea ice friction do explain the observed seasonal change, and the blockage is not required. The observed changes are likely a combination of large sea ice friction and a sea ice blockage in Victoria Strait of variable thickness.

References

Bruno, M., Blumberg, A. and Herrington, T. (2006). The urban ocean observatory—Coastal ocean observations and forecasting in the New York Bight. *Journal of Marine Science Environment*, C4, pp.1-9.

Chen, C., Beardsley, R. and Cowles, G. (2006). An Unstructured Grid, Finite-Volume Coastal Ocean Model (FVCOM) System. *Oceanography*, 19(1), pp.78-89.

Chen, C., Gao, G., Qi, J., Proshutinsky, A., Beardsley, R. C., Kowalik, Z., Lin, H. and Cowles, G. (2009). A new high-resolution unstructured grid finite volume Arctic Ocean model (AO-FVCOM): An application for tidal studies, *Journal of Geophysical Research*, 114, C08017.

Chen, C., Liu, H. and Beardsley, R. (2003). An Unstructured Grid, Finite-Volume, Three-Dimensional, Primitive Equations Ocean Model: Application to Coastal Ocean and Estuaries. *Journal of Atmospheric and Oceanic Technology*, 20(1), pp.159-186.

Collins, A., Hannah, C. and Greenberg, D. (2011). Validation of a high resolution modelling system for tides in the Canadian Arctic Archipelago. *Canadian Technical Report of Hydrography and Ocean Sciences*, 273, vii + 72 pp.

Cummins, P., Karsten, R. and Arbic, B. (2010). The semi-diurnal tide in Hudson strait as a resonant channel oscillation. *Atmosphere-Ocean*, 48(3), pp.163-176.

Dierking, W. (2013). Sea Ice Monitoring by Synthetic Aperture Radar. *Oceanography*, 26(2).

Egbert, G. and Erofeeva, S. (2002). Efficient Inverse Modeling of Barotropic Ocean Tides. *Journal of Atmospheric and Oceanic Technology*, 19(2), pp.183-204.

Egbert, G., and Ray, R. (2001). Estimates of M_2 tidal energy dissipation from TOPEX/Poseidon altimeter data. *Journal of Geophysical Research*, 106(C10), pp.22475– 22502.

Foreman, M. and Henry, R. (1989). The harmonic analysis of tidal model time series. *Advances in Water Resources*, 12, pp. 109-120.

Foreman, M. and Neufeld, E. (1991). Harmonic tidal analyses of long time series. *International Hydrographic Review*, 68, pp.85–108.

Georgas, N. (2012). Large Seasonal Modulation of Tides due to Ice Cover Friction in a Midlatitude Estuary*. *Journal of Physical Oceanography*, 42(3), pp.352-369.

Godin, G. (1986). Modification by an Ice Cover of the Tide in James Bay and Hudson Bay. *ARCTIC*, 39(1).

Haas, C. and Howell, S. (2015). Ice thickness in the Northwest Passage. *Geophysical Research Letters*, 42(18), pp.7673-7680.

Haas, C., Lobach, J., Hendricks, S., Rabenstein, L. and Pfaffling, A. (2009). Helicopter-borne measurements of sea ice thickness, using a small and lightweight, digital EM system. *Journal of Applied Geophysics*, 67(3), pp.234-241.

Hannah, C., Dupont, F. and Dunphy, M. (2009). Polynyas and Tidal Currents in the Canadian Arctic Archipelago. *ARCTIC*, 62(1).

Henry, R., and Foreman, M. (2001). A Representation of Tidal Currents Based on Energy Flux, *Marine Geodesy*, 24:3, pp.139-152.

Holloway, G. and Proshutinsky, A. (2007). Role of tides in Arctic ocean/ice climate. *Journal of Geophysical Research*, 112(C4).

Iceweb1.cis.ec.gc.ca. (2019). *Ice Graph*. [online] Available at: https://iceweb1.cis.ec.gc.ca/IceGraph/page1.xhtml?lang=en [Accessed 23 May 2018].

Isdm-gdsi.gc.ca. (2019). *Integrated Science Data Management (ISDM)*. [online] Available at: http://www.isdm-gdsi.gc.ca/isdm-gdsi/twl-mne/inventory-inventaire/index-eng.htm [Accessed 8 Mar. 2019].

Johnston, M., & Haas, C. (2011). Proceedings of the 21st International Conference on Port and Ocean Engineering under Arctic Conditions, POAC'11, POAC11-132. In *The 21st International Conference on Port and Ocean Engineering under Arctic Conditions*. Montréal.

Kagan, B. and Sofina, E. (2010). Ice-induced seasonal variability of tidal constants in the Arctic Ocean. *Continental Shelf Research*, 30(6), pp.643-647.

Kagan, B. and Sofina, E. (2012). Spatial structure of the M2 tidal wave in the Canadian Arctic Archipelago. *Izvestiya, Atmospheric and Oceanic Physics*, 48(2), pp.241-253.

Kagan, B. and Timofeev, A. (2006). Tidal ice drift in the White Sea: Results of a numerical experiment. *Oceanology*, 46(6), pp.796-802.

Kagan, B., Sofina, E. and Timofeev, A. (2011). Modeling of the M2 surface and internal tides and their seasonal variability in the Arctic Ocean: Dynamics, energetics and tidally induced diapycnal diffusion. *Journal of Marine Research*, 69(2), pp.245-276.

Kagan, B., Timofeev, A. and Sofina, E. (2010). Seasonal variability of surface and internal M2 tides in the Arctic Ocean. *Izvestiya, Atmospheric and Oceanic Physics*, 46(5), pp.652-662.

Kleptsova, O. and Pietrzak, J. (2018). High resolution tidal model of Canadian Arctic Archipelago, Baffin and Hudson Bay. *Ocean Modelling*, 128, pp.15-47.

Kowalik, Z. (1981). A Study of the M-2 Tide in the Ice-Covered Arctic Ocean. *Modeling, Identification and Control: A Norwegian Research Bulletin*, 2(4), pp.201-223.

Kowalik, Z. and Proshutinsky, A. (1993). Diurnal tides in the Arctic Ocean. *Journal of Geophysical Research*, 98(C9), p.16449.

Kowalik, Z. and Proshutinsky, A. (1994). The Arctic Ocean Tides. *The Polar Oceans and Their Role in Shaping the Global Environment*, pp.137-158.

Kulikov, M., Medvedev, I. and Kondrin, A. (2018). Seasonal variability of tides in the Arctic Seas. *Russian Journal of Earth Sciences*, 18(5), pp.1-14.

Langleben, M. (1982). Water drag coefficient of first-year sea ice. *Journal of Geophysical Research*, 87(C1), p.573.

LeBlond, P., & Mysak, L. (1978). *Waves in the ocean*. Amsterdam: Elsevier Scientific Pub. Co.

Lee, J. (1971). Wave-induced oscillations in harbours of arbitrary geometry. *Journal of Fluid Mechanics*, 45(02), p.375.

Lu, P., Li, Z., Cheng, B. and Leppäranta, M. (2011). A parameterization of the ice-ocean drag coefficient. *Journal of Geophysical Research*, 116(C7).

Luettich, R., & Westerink, J. (2004). *Formulation and numerical implementation of the 2D/3D ADCIRC finite element model version 44. XX*. [Morehead City, N.C.?]: [R. Luettich?].

Luneva, M., Aksenov, Y., Harle, J. and Holt, J. (2015). The effects of tides on the water mass mixing and sea ice in the Arctic Ocean. *Journal of Geophysical Research: Oceans*, 120(10), pp.6669-6699.

Madsen, O. and Bruno, M. (1987). A Methodology for the Determination of Drag Coefficients for Ice Floes. *Journal of Offshore Mechanics and Arctic Engineering*, 109(4), p.381.

Melling, H. (2002). Sea ice of the northern Canadian Arctic Archipelago. *Journal of Geophysical Research*, 107(C11).

Miles, J. and Lee, Y. (1975). Helmholtz resonance of harbours. *Journal of Fluid Mechanics*, 67(3), pp.445-464.

Mullarney, J., Hay, A. and Bowen, A. (2008). Resonant modulation of the flow in a tidal channel. *Journal of Geophysical Research*, 113(C10).

Müller, M., Cherniawsky, J., Foreman, M. and von Storch, J. (2012). Global M2 internal tide and its seasonal variability from high resolution ocean circulation and tide modeling. *Geophysical Research Letters*, 39(19), p.L19607

Müller, M., Cherniawsky, J., Foreman, M. and von Storch, J. (2014). Seasonal variation of the M 2 tide. *Ocean Dynamics*, 64(2), pp.159-177.

Munk, W., Zetler, B. and Groves, G. (1965). Tidal Cusps. *Geophysical Journal International*, 10(2), pp.211-219.

Nsidc.org. (2019). *Charctic Interactive Sea Ice Graph | Arctic Sea Ice News and Analysis*. [online] Available at: https://nsidc.org/arcticseaicenews/charctic-interactive-sea-ice-graph/ [Accessed 12 Mar. 2019].

Padman, L. and Erofeeva, S. (2004). A barotropic inverse tidal model for the Arctic Ocean. *Geophysical Research Letters*, 31(2).

Pairaud, I., Lyard, F., Auclair, F., Letellier, T. and Marsaleix, P. (2008). Dynamics of the semi-diurnal and quarter-diurnal internal tides in the Bay of Biscay. Part 1: Barotropic tides. *Continental Shelf Research*, 28(10-11), pp.1294-1315.

Pawlowicz, R., Beardsley, B. and Lentz, S. (2002). Classical tidal harmonic analysis including error estimates in MATLAB using T_TIDE. *Computers & Geosciences*, 28(8), pp.929-937.

Pease, C., Salo, S. and Overland, J. (1983). Drag measurements for first-year sea ice over a shallow sea. *Journal of Geophysical Research*, 88(C5), p.2853.

Platzman, G. (1972). Two-Dimensional Free Oscillations in Natural Basins. *Journal of Physical Oceanography*, 2(2), pp.117-138.

Prinsenberg, S. (1988). Damping and Phase Advance of the Tide in Western Hudson Bay by the Annual Ice Cover. *Journal of Physical Oceanography*, 18(11), pp.1744-1751.

St-Laurent, P., Saucier, F. and Dumais, J. (2008). On the modification of tides in a seasonally ice-covered sea. *Journal of Geophysical Research*, 113(C11).

Tsamados, M., Feltham, D., Schroeder, D., Flocco, D., Farrell, S., Kurtz, N., Laxon, S. and Bacon, S. (2014). Impact of Variable Atmospheric and Oceanic Form Drag on Simulations of Arctic Sea Ice*. *Journal of Physical Oceanography*, 44(5), pp.1329-1353.

Varela, D., Crawford, D., Wrohan, I., Wyatt, S. and Carmack, E. (2013). Pelagic primary productivity and upper ocean nutrient dynamics across Subarctic and Arctic Seas. *Journal of Geophysical Research: Oceans*, 118(12), pp.7132-7152.

Volkov, V., Johannessen, O., Borodachev, V., Voinov, N., Pettersson, H., Bobylev, P. and Kouraev, V. (2002). *Polar seas oceanography: An integrated case study of the Kara Sea*. London: Springer.

Williams, W., Carmack, E. and Ingram, R. (2007). Chapter 2 Physical Oceanography of Polynyas. In: W. Smith and D. Barber, ed., *Polynyas: Windows to the World*. Elsevier Science & Technology, pp.55-85.

Wu, Y., Chaffey, J., Greenberg, D. and Smith, P. (2015). Environmental Impacts Caused by Tidal Power Extraction in the Upper Bay of Fundy. *Atmosphere-Ocean*, 54(3), pp.326-336.

Wu, Y., Chaffey, J., Law, B., Greenberg, D., Drozdowski, A., Page, F. and Haigh, S. (2014). A three-dimensional hydrodynamic model for aquaculture: a case study in the Bay of Fundy. *Aquaculture Environment Interactions*, 5(3), pp.235-248.